



TAMPERE UNIVERSITY OF TECHNOLOGY

Department of Electrical Energy Engineering

TUOMAS MESSO

DYNAMIC CHARACTERIZATION OF THREE-PHASE INVERTER IN PHOTOVOLTAIC APPLICATIONS

Master of Science Thesis

Examiner: Teuvo Suntio

The examiner and the topic were approved in the Faculty of Computing and Electrical Engineering Council meeting on 6.4.2011

TIIVISTELMÄ

TAMPEREEN TEKNILLINEN YLIOPISTO

Sähkötekniikan diplomi-insinöörin tutkinto

TUOMAS MESSO: Dynamic characterization of three-phase inverter in photovoltaic applications

Diplomityö, 59 sivua, 5 liitesivua

Syyskuu 2011

Pääaine: Teholähde-elektronikka

Tarkastaja: Prof. Teuvo Suntio

Avainsanat: aurinkosähköjärjestelmä, jännite-syöttöinen vaihtosuuntaaja, dynamiikka, mallinnus, säätösuunnittelu

Tehoelektronikkaa käytetään rajapintana liitettäessä uusiutuvia energialähteitä jakeluverkkoon. Aurinkopaneeli tuottaa tasasähköä ja se on liitettävä jakeluverkkoon kolmivaiheisen vaihtosuuntaajan avulla. Se on rakenteeltaan virtalähde, jonka virta-jännitekäyttäytyminen on epälineaarista. Aurinkopaneelin ominaisuuksilla on suuri vaikutus vaihtosuuntaajan dynamiikkaan, vaikka tätä ei kirjallisuudessa usein huomioida.

Teholähteet ovat yleensä säädettyjä järjestelmiä. Aurinkosähkösovelluksissa esimerkiksi paneelin jännite pidetään sopivana tehontuoton maksimoimiseksi. Säättöjärjestelmä on viritettävä siten, että se on stabiili ja riittävän nopea. Tämän saavuttamiseksi teholähteen piensignaalikäyttäytyminen on syytä tuntea.

Tavanomaisessa piensignaalmallinnuksessa ratkaistaan teholähteen toimintapiste ja tutkitaan toimintaa tämän pisteen ympäristössä. Vaihtosuuntaajan tapauksessa tämä ei ole mahdollista, sillä osa suureista on sinimuotoisia. Mallinnus voidaan kuitenkin tehdä hyödyntämällä avaruusvektorteoriaa. Sinimuotoiset suureet muunnetaan verkko-taajuudella pyörivään avaruusvektori-koordinaatistoon, jolloin niistä tulee tasasuureita ja toimintapiste voidaan ratkaista. Edellisen tuloksena saatava malli on kuitenkin hyvin monimutkainen, jonka vuoksi suljetun järjestelmän siirtofunktioita ei pystytäkään ratkaisemaan. Tässä työssä kehitettiin yksinkertaistettu malli kolmivaiheiselle vaihtosuuntaajalle, josta myös suljetun järjestelmän siirtofunktiot on mahdollista ratkaista. Mallin pätevyys varmennettiin simulointimallien ja taajuusvaste-analyysin avulla. Lopuksi rakennettiin prototyyppi, josta taajuusvasteet voitiin mitata.

Aurinkopaneelin vaikutusta teholähteen piensignaalikäyttäytymiseen tutkittiin prototyypin avulla. Saatujen tulosten perusteella paneelilla on suuri vaikutus vaihtosuuntaajaan erityisesti säätösuunnittelun kannalta. Tärkeimmät tulokset olivat oikean puolitason nollan ilmestyminen teholähteen dynamiikkaan sekä negatiivinen lähtöimpedanssi käytettäessä kaskadisäätöä. Kaskadisäätöä käytetään jakeluverkon kytketyissä säätöjärjestelmissä tehontuoton maksimoimiseksi. Negatiivinen lähtöimpedanssi voi aiheuttaa stabiilisuusongelmia ja huonontaa verkon vaimennusta.

ABSTRACT

TAMPERE UNIVERSITY OF TECHNOLOGY

Master's Degree Programme in Electrical Engineering

TUOMAS MESSO: Dynamic characterization of three-phase inverter in photovoltaic applications

Master of Science Thesis, 59 pages, 5 Appendix pages

September 2011

Major: Switched-mode power supplies

Examiner: Prof. Teuvo Suntio

Keywords: photovoltaic, VSI, three-phase inverter, dynamics, modeling, control design

Power electronic devices are used as an interface between renewable energy sources and the utility grid. A photovoltaic generator that produces dc electricity is interfaced to a three-phase grid with an inverter. A photovoltaic generator is internally a current source that has highly nonlinear terminal characteristics. The properties of the input source has a great impact on the converter dynamics, which is seldom recognized.

Electrical quantities of a power electronic converter are usually regulated to a desired level. This task is laid on the control system which should be tuned to achieve good regulation and disturbance rejection. The knowledge of the converter's small-signal behavior is a great advantage in the control system design.

Conventional small-signal modeling can not be performed in the case of dc-ac converters due to the fact that some of the quantities are sinusoidal by nature and thus have no steady-state solutions. Nevertheless, small-signal modeling of a three-phase inverter can be done if the three-phase variables are transformed into a synchronous reference frame. However, such a model becomes quite complex and e.g. closed-loop transfer functions can not be solved with reasonable effort. In this thesis, a reduced order model is developed based on a dc-dc equivalence of the inverter. The validity of reduced order model was verified by comparing the inverter transfer functions with the proposed model using a simulation model and frequency response analysis. A prototype was constructed and results were verified by comparing measured and predicted frequency responses.

The effect of a photovoltaic generator on the converter dynamics was examined. It was found out that the photovoltaic generator has a profound effect on the small-signal characteristics of the converter especially from the control design point of view. Most important results were the appearance of a right-half-plane zero in control dynamics and negative output impedance with a typical cascaded control scheme. Such a control system has to be implemented in grid-connected photovoltaic systems in order to transfer maximum power to the grid. The negative output impedance can impose stability problems in the converter-grid-interface and reduce damping in the grid.

PREFACE

The master thesis was done for the Department of Electrical Energy Engineering during year 2011 to a topic suggested by Prof. Teuvo Suntio. The supervisor of the work was M.Sc. Joonas Puukko and the examiner Prof. Teuvo Suntio. The prototype converter was designed and assembled by M.Sc. Juha Huusari and the DSP coding and measurements mainly by M.Sc. Lari Nousiainen.

I want to address my gratitude especially to M.Sc. Joonas Puukko for a great introduction to the theory behind the work and hints through the most difficult subjects. I want to also thank Prof. Teuvo Suntio for inspiration and guidance through the whole process. Finally I want to thank the rest of the team, M.Sc. Anssi Mäki, M.Sc. Diego Torres Lobera, M.Sc. Jari Leppäaho, M.Sc. Juha Huusari and M.Sc. Lari Nousiainen for a great working environment.

Tampere 1.8.2011

Tuomas Messo

CONTENTS

1. Introduction	1
2. Small-signal modeling of switched-mode dc-dc converters	4
2.1 Different conversion schemes	4
2.2 Averaged model	5
2.3 Linearized state-space model	7
2.4 Source and load effects	9
3. Space-vector theory	12
4. Small-signal modelling of three-phase inverters	15
4.1 Three-phase inverter	15
4.2 Control of a three-phase inverter	17
4.3 Averaged model in the synchronous reference frame	18
4.4 Linearized state-space model in the synchronous reference frame	22
5. Dynamics of a dc-equivalent converter	27
5.1 Open-loop transfer functions	28
5.2 Closed-loop transfer functions	33
6. Effect of photovoltaic generator on converter dynamics	38
6.1 Electrical properties of a photovoltaic cell	38
6.2 Effect of photovoltaic generator on open-loop dynamics	39
6.3 Control system design	42
6.4 Effect of a photovoltaic generator on closed-loop dynamics	46
7. Conclusions	49
Bibliography	51
A.Comparison of inverter and reduced order models	55
B.Closed-loop output impedances of dc-equivalent circuit	57
C.Prototype converter	58

TERMS AND SYMBOLS

GREEK ALPHABET

α	Real component in stationary reference frame
β	Imaginary component in stationary reference frame
Δ	Characteristic polynomial
Θ	Phase angle of the grid voltage
ω_{p-in}	Input voltage controller pole angular frequency
ω_{p-out}	Output current controller pole angular frequency
ω_s	Grid fundamental angular frequency
ω_{z-in}	Input voltage controller zero angular frequency
ω_{z-out}	Output current controller zero angular frequency

LATIN ALPHABET

A	System matrix
B	Input matrix
C	Output matrix
<i>C</i>	Capacitance
C_{sh}	Parasitic capacitance of a PV cell
<i>d</i>	Duty ratio
d'	Complement of the duty ratio
D	Input-output matrix
<i>D</i>	Steady-state value of duty ratio
d_i	Duty ratio of upper switch of an inverter phase leg
\underline{d}	Space-vector transformed duty ratio
\underline{d}^s	Space-vector transformed duty ratio in synchronous reference frame
d_d	Direct component of duty ratio
d_q	Quadrature component of duty ratio
D_d	Steady-state value of duty ratio's direct component
D_q	Steady-state value of duty ratio's quadrature component
u_{oL}	Load voltage of non-ideal load
G_a	Gain of the pulse width modulator
G_{ca}	Current controller transfer function
G_{cc}	Voltage controller transfer function
G_{cd}	D-channel current controller transfer function
G_{ci-o}	Open-loop control-to-input transfer function
G_{ci-o}^s	Source-affected open-loop control-to-input transfer function
G_{ci-d}	D-channel open-loop control-to-input transfer function
G_{ci-q}	Q-channel open-loop control-to-input transfer function
G_{co-o}	Open-loop control-to-output transfer function
G_{co-o}^s	Source-affected open-loop control-to-output transfer function
G_{co-d}	D-channel open-loop control-to-output transfer function
G_{co-dq}	D-channel to q-channel open-loop control-to-output transfer function
G_{co-q}	Q-channel open-loop control-to-output transfer function
G_{co-qd}	Q-channel to d-channel open-loop control-to-output transfer function
G_{cr-dq}	D-channel to q-channel cross-coupling transfer function at open loop
G_{cr-qd}	Q-channel to d-channel cross-coupling transfer function at open loop
G_{cq}	Q-channel current controller transfer function

\mathbf{G}_H	Matrix containing transfer functions of a current-to-current converter
G_{io-o}	Open-loop input-to-output transfer function
G_{io-d}	D-channel open-loop input-to-output transfer function
G_{io-q}	Q-channel open-loop input-to-output transfer function
$G_{io-\infty}$	Ideal input-to-output transfer function
i_C	Capacitor current
i_d	Diode current
i_{in}	Input current of the converter
i_o	Output current of the converter
i_L	Inductor current
I_L	Steady-state value of inductor current
\underline{i}_L	Space-vector transformed inductor current
\underline{i}_L^s	Space-vector transformed inductor current in synchronous frame
\underline{i}_{Li}	Inductor current of phase i
i_{Ld}	Inductor current d-component
I_{Ld}	Inductor current d-component steady-state value
i_{Lq}	Inductor current q-component
i_{inS}	Input current of a non-ideal source
$\langle x \rangle$	Average value of variable x
\hat{x}	AC-perturbation around a steady-state operation point
\dot{x}	Time derivative of variable x
$\underline{\mathbf{x}}$	Space-vector
$\underline{\mathbf{x}}^*$	Complex-conjugate of a space-vector
\mathbf{I}	Identity matrix
K_{in}	Input voltage controller gain
K_{out}	Output current controller gain
L	Inductance
L_{in}	Input voltage control loop
L_{out}	Output current control loop
s	Laplace variable
T_s	Switching period
T_{oi}	Output-to-input transfer function
$T_{oi-\infty}$	Ideal output-to-input transfer function
\mathbf{U}	Vector containing Laplace transformed input variables
\mathbf{u}	Vector containing input variables
\mathbf{x}	Vector containing state variables
\mathbf{Y}	Vector containing Laplace transformed output variables
\mathbf{y}	Vector containing output variables
Y_o	Output admittance
Y_{o-d}	D-channel output admittance
Y_{o-q}	Q-channel output admittance
Y_{o-sci}	Short-circuit output admittance
$Y_{o-\infty}$	Ideal output admittance
Y_S	Output admittance of a non-ideal source
Z_{in-oco}	Open circuit input impedance
$Z_{in-\infty}$	Ideal input impedance
d	Direct component of a space-vector transformed variable
q	Quadrature component of a space-vector transformed variable

Z_{in}	Input impedance
Z_L	Load impedance

ABBREVIATIONS

<i>AC</i>	Alternating current
<i>CC</i>	Constant current
<i>CCM</i>	Continuous conduction mode
<i>CF</i>	Current-fed
<i>CV</i>	Constant voltage
<i>CO₂</i>	Carbon-dioxide
<i>DC</i>	Direct current
<i>DCM</i>	Discontinuous conduction mode
<i>KCL</i>	Kirchoff current law
<i>KVL</i>	Kirchoff voltage law
<i>MPP</i>	Maximum power point
<i>MPPT</i>	Maximum power point tracking
<i>OC</i>	Open-circuit
<i>PLL</i>	Phase-locked loop
<i>PV</i>	Photovoltaic
<i>PWM</i>	Pulse width modulation
<i>RHP</i>	Right-half plane
<i>SC</i>	Short-circuit
<i>SVMPWM</i>	Space-vector pulse width modulation
<i>VSI</i>	Voltage sourced inverter

1. INTRODUCTION

It is a known fact that burning of fossil fuels releases pollutant gases to the atmosphere. The most critical product of these greenhouse gases is the carbondioxide, which is partly responsible for the global warming effect. Scientists have studied the concentration of CO_2 in the atmosphere over a long period of time by ice core studies. It is undeniable that the rise of CO_2 concentration is due to human activities. Burning of fossil fuel produces 8,000 million metric tons of CO_2 per year of which 50% is due to electric power generation. It has been predicted that the rise of global temperature in the next 100 years is somewhere between 2 and 5 degrees celcius. The rising temperature causes droughts which make acricultural production more difficult, damages vegetation and reduces fresh water supplies. This will be problematic especially in areas near the equator. A more serious effect is the melting of glaciers all over the world. According to worst-case scenarios, this could raise the sea level by nearly one meter in the next 100 years. This is an alarming observation, since about 100 million people live within one meter elevation of sea level.[1]

It is evident that nowadays people are more concerned about drawbacks related to the use of fossil fuels. This has given rise to new clean renewable energy technologies such as solar, wind, and hydro power [2–4]. Hydro energy includes also tidal and wave energy. Wind energy can be harnessed with windmills and converted into electrical energy. Solar energy can be converted to electrical energy directly with solar cells or indirectly with solar thermal power plants.

A photovoltaic cell (PV) is the basic building block of a larger electrical system. The voltage produced by a single PV cell is usually less than one volt and has to be boosted by connecting enough cells in series. This arrangement is called a photovoltaic module. These in turn are connected in series and parallel to match the voltage and current required by the load system. The resulting electrical system is addressed as a photovoltaic generator in this thesis.

The use of power electronic devices plays an essential role in exploiting all of the known renewable energy sources. Dc-dc converters can be used for maximizing the energy generation and boosting the low voltage of solar generators. Ac-ac converters are used in wind power applications to extract maximum amount of the available wind energy. Dc-ac converters are used to transform electrical energy to a form that can be injected to the utility grid and consumed elsewhere.

Some of the electrical quantities of power electronic devices are usually controlled, e.g. input voltage in photovoltaic applications has to be controlled in order to extract maximum power from the PV generator. Negative feedback control is usually used to achieve desired regulation performance. One of the main issues with power electronics

is to assure the overall stability of the control system. Design of stable feedback loops require that the small-signal behavior of the converter is known. Small-signal model is usually transformed to frequency or Laplace domain where the magnitude and phase behavior of the frequency responses can be studied.[5]

Solar energy seems to be one of the most promising renewable energy technologies at the moment. In grid-connected systems, the dc current produced by the PV generator needs to be transformed to three-phase current fed to the ac power grid. Two possible ways to achieve this is to use single or two-stage approach as depicted in Fig. 1.1.

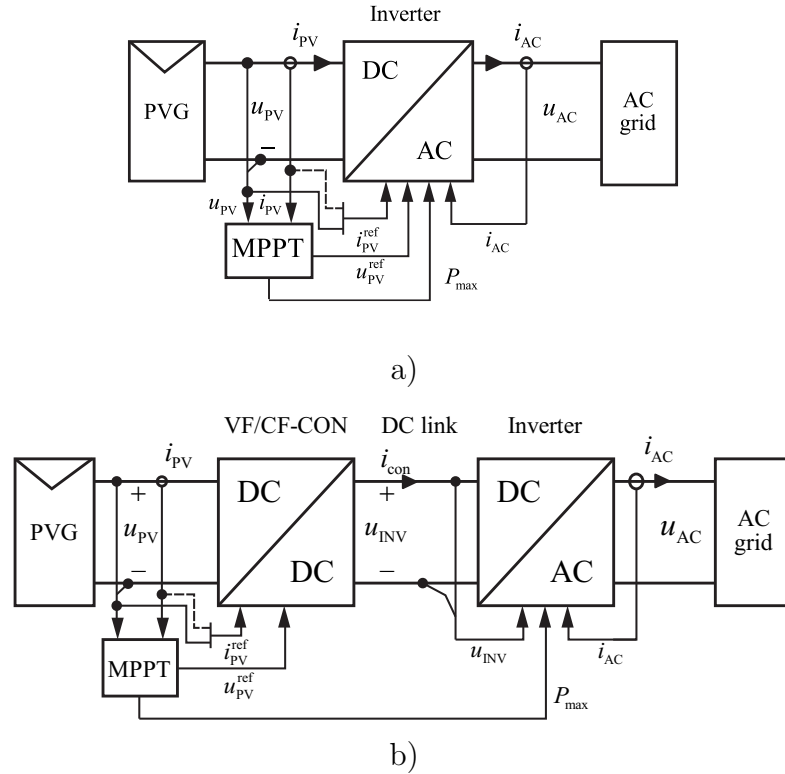


Figure 1.1: a) Single b) and two-stage interfacing scheme.

In Fig 1.1b, the voltage of the PV generator is adjusted by the dc-dc converter and the three-phase dc-ac converter accounts for the grid connection. In this case the PV generator voltage can be boosted by the dc-dc converter to an appropriate level. The second option in Fig 1.1a includes only an ac-dc stage, which is responsible of both, the generator voltage regulation and grid connection. Using only an ac-dc converter reduces losses but the drawback is that because there is no voltage boosting dc-dc stage more PV cells need to be connected in series to reach voltage required by the grid connection. In either case, the ac-dc converter is an essential part of the system.

In order to assure a stable control of the ac-dc converter, its small-signal behavior has to be known. A multitude of articles dealing with the dynamics of three-phase dc-ac converter are presented in the literature [6–12]. In majority of these, the photovoltaic interfacing inverter is fed by a constant voltage source. In some of them, the linearization step is not done in respect to every variable, e.g. duty ratio or the input

voltage is treated as a constant. The photovoltaic cell is internally a current source and has highly non-linear and non-ideal terminal characteristics [13]. Such a behavior has a great effect on the inverter dynamics. Hence, the inverter should be modeled with a correct type of input source.

In this thesis, the small-signal behavior of a two-level three-phase inverter used as an interface between utility grid and a PV generator is studied. Chapter 2 gives a short review in conventional small-signal analysis where the dynamics of a current-fed dc-dc converter is studied as an example. Chapter 3 recaps space-vector theory associated with three-phase systems and Chapter 4 combines two previous chapters to formulate a small-signal model for a three-phase two-level inverter in the synchronous reference frame. In Chapter 5, the inverter model is simplified to a dc-equivalent model, which has the same dynamical properties as the inverter model in the synchronous reference frame. Chapter 6 presents the measurements from the DC-equivalent converter prototype and the effect of the photovoltaic generator on the dynamics is studied. Issues related to control design are also discussed. The final chapter concludes the thesis and the most important results are recapped.

2. SMALL-SIGNAL MODELING OF SWITCHED-MODE DC-DC CONVERTERS

A dc-dc converter is a nonlinear system due to different subcircuits introduced by the switching action. Hence, methods for linear system analysis, such as Laplace transformation usually applied in control theory are unusable. A general approach to overcome this is to capture the average behavior of the converter over one switching period and then linearize the resulting system at a predefined operating point. The small-signal modeling method for dc-dc converters was first introduced by Middlebrook in the 70's. This topic has been extensively studied in the literature [14–16] ever since.

2.1 Different conversion schemes

Source and load, whether voltage or current type, have a great influence on the behavior of electrical systems especially from the dynamical point of view. Input voltage of a converter connected to a constant voltage source cannot be controlled, because it is determined by the source itself. Same is true for the load, i.e. the output current cannot be controlled if the load is a current sink. Converters can be categorized to four main types depending on the type of source and load: voltage-to-voltage, voltage-to-current, current-to-current and current-to-voltage converters. A photovoltaic dc-dc converter, e.g. is usually a current-fed converter. It converts the current generated by the PV panel into a current or voltage fed to the load. Usually the load is a counter voltage, i.e. a storage battery, in which case the PV converter acts as a current-to-current converter. The four main conversion schemes are summarized in Fig. 2.1.

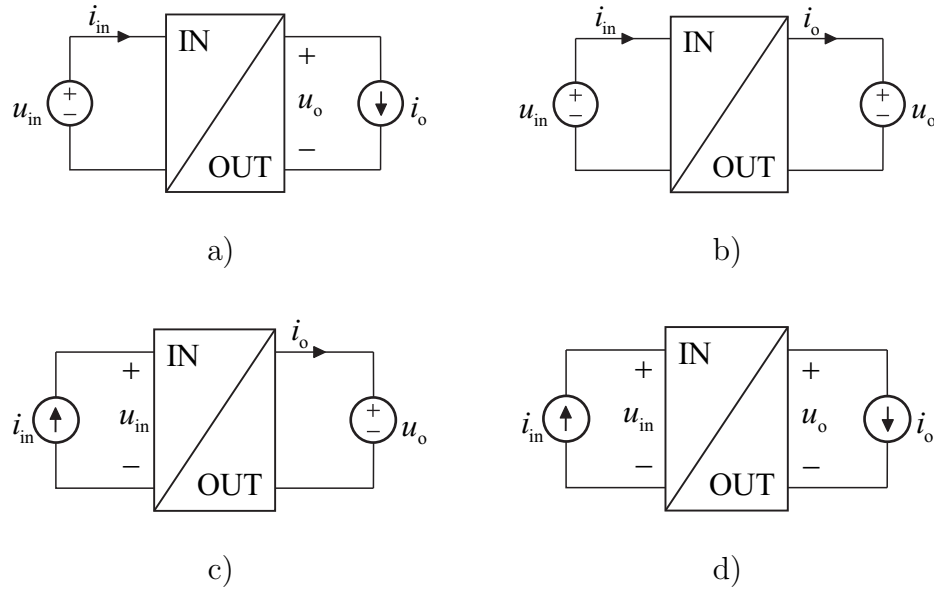


Figure 2.1: Classification of conversion schemes: a) voltage-to-voltage, b) voltage-to-current, c) current-to-current and d) current-to-voltage.

2.2 Averaged model

A switched-mode converter is actually a combination of different subcircuits. The number of subcircuits depends on the operation mode of the converter. In constant conduction mode (CCM) inductor current either rises or falls depending on the switching-state and never drops to zero, thus the number of subcircuits is two. In discontinuous conduction mode (DCM) the number of subcircuits is increased to three, because the inductor current drops to zero at the end of each switching period. For simplicity of analysis and the scope of this thesis, operation in DCM is not discussed. As an example, a current-fed dc-dc converter depicted in Fig. 2.2 is studied. The topology is derived from a buck-type power stage by adding an input capacitor. Such a topology can be used e.g. as an interfacing dc-dc converter for a photovoltaic generator. On- and off-time subcircuits resulting from the switching action of the converter in Fig. 2.2 are presented in Fig. 2.3. Parasitic elements are omitted, because the purpose of this chapter is just to provide a short introduction over the modeling method.

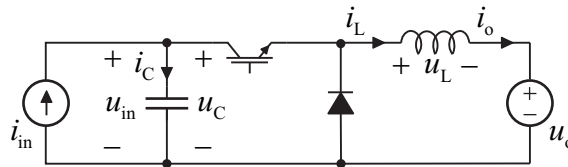


Figure 2.2: Power stage of a current-fed dc-dc converter.

Inductor voltage and capacitor current equations can be extracted from the two subsystems by means of Kirchhoff's voltage (KVL) and current (KCL) laws. The

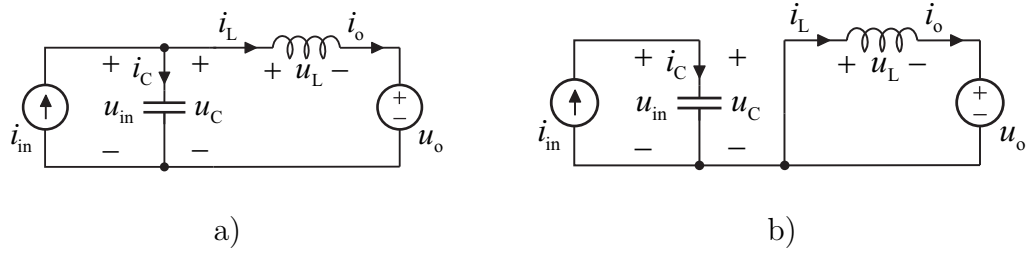


Figure 2.3: a) On-time and b) off-time subcircuit of the converter.

input variables of the converter are the input current i_{in} and the output voltage u_o . The output variables are defined by source and load types: in the case of Fig. 2.2 the controllable output variables are the input voltage u_{in} and the output current i_o . The state variables are the inductor current i_L and the input capacitor voltage u_C . L is the inductance of the output inductor and C the capacitance of the input capacitor. Resulting equation sets for on- and off-time circuits are presented in (2.1) and (2.2).

$$\begin{aligned}
 \frac{di_{L,\text{on}}}{dt} &= \frac{u_C}{L} - \frac{u_o}{L} \\
 \frac{du_{C,\text{on}}}{dt} &= \frac{i_{\text{in}}}{C} - \frac{i_L}{C} \\
 u_{\text{in,on}} &= u_C \\
 i_{o,\text{on}} &= i_L
 \end{aligned} \tag{2.1}$$

$$\begin{aligned}
 \frac{di_{L,\text{off}}}{dt} &= -\frac{u_o}{L} \\
 \frac{du_{C,\text{off}}}{dt} &= \frac{i_{\text{in}}}{C} \\
 u_{\text{in,off}} &= u_C \\
 i_{o,\text{off}} &= i_L
 \end{aligned} \tag{2.2}$$

The next step is to average the converter behavior over one switching period. In the field of power electronics, it is customary to denote an average value of a signal by anglebrackets. The average value of any signal can be mathematically expressed as

$$\langle x \rangle = \frac{1}{T} \int_0^T x(t) dx. \tag{2.3}$$

Equation sets can be averaged over one switching period by taking an integral over the whole switching period which includes both subcircuits. This is equivalent to multiplying the on-time equations by the duty ratio d and the off-time equations by the complement of the duty ratio d' . Resulting average valued state-space model is as

shown in (2.4).

$$\begin{aligned}
 \frac{d \langle i_L \rangle}{dt} &= \frac{d \langle u_C \rangle}{L} - \frac{\langle u_o \rangle}{L} \\
 \frac{d \langle u_C \rangle}{dt} &= \frac{\langle i_{in} \rangle}{C} - \frac{d \langle i_L \rangle}{C} \\
 \langle u_{in} \rangle &= \langle u_C \rangle \\
 \langle i_o \rangle &= \langle i_L \rangle
 \end{aligned} \tag{2.4}$$

It can be immediately seen that the resulting model is nonlinear due to terms $d \langle u_C \rangle$ and $d \langle i_L \rangle$. This model can be used for simulation purposes, although it does not contain information about the switching ripple. However, the averaged model becomes useful in the following analysis, because the steady-state operating point needed for the linearization step can be solved from it.

2.3 Linearized state-space model

In order to use mathematical tools, such as Laplace transformation, the averaged nonlinear model derived above needs to be linearized. The linearization can be done as in [14], by denoting the average values of (2.4) by a constant dc value summed with a small ac-perturbation. However, in control engineering it is customary to linearize nonlinear equations with first-order partial derivatives at a desired operating point[17]. The steady-state operating point can be solved from the averaged model (2.4) by noticing that the differential terms equal to zero at steady state.

As an example, the equation $f = d \langle u_C \rangle / L$ can be linearized by first treating the duty ratio as a constant and solving the derivative in respect to capacitor voltage and then considering the capacitor voltage as a constant and solving the derivate in respect to duty ratio. Resulting first-order partial derivatives are shown in (2.5), where D and U_C are the steady-state values for duty ratio and capacitor voltage obtained from the averaged model.

$$\begin{aligned}
 \frac{\partial f \hat{u}_C}{\partial \langle u_C \rangle} &= \frac{D}{L} \\
 \frac{\partial f \hat{d}}{\partial d} &= \frac{U_C}{L}
 \end{aligned} \tag{2.5}$$

Solving the steady-state values for capacitor voltage and inductor current and linearizing (2.4) gives a linearized state-space representation as shown in (2.6).

$$\begin{aligned}
\frac{d\hat{i}_L}{dt} &= \frac{D}{L}\hat{u}_C - \frac{1}{L}\hat{u}_o + \frac{U_{in}}{L}\hat{d} \\
\frac{d\hat{u}_C}{dt} &= -\frac{D}{C}\hat{i}_L + \frac{1}{C}\hat{i}_{in} - \frac{I_{in}}{DC}\hat{d} \\
\hat{u}_{in} &= \hat{u}_C \\
\hat{i}_o &= \hat{i}_L
\end{aligned} \tag{2.6}$$

The linearized state-space model can be presented in a matrix form by

$$\begin{bmatrix} \frac{d\hat{i}_L}{dt} \\ \frac{d\hat{u}_C}{dt} \end{bmatrix} = \begin{bmatrix} 0 & \frac{D}{L} \\ -\frac{D}{C} & 0 \end{bmatrix} \begin{bmatrix} \hat{i}_L \\ \hat{u}_C \end{bmatrix} + \begin{bmatrix} 0 & -\frac{1}{L} & \frac{U_{in}}{L} \\ \frac{1}{C} & 0 & -\frac{I_{in}}{DC} \end{bmatrix} \begin{bmatrix} \hat{i}_{in} \\ \hat{u}_o \\ \hat{d} \end{bmatrix}, \tag{2.7}$$

$$\begin{bmatrix} \hat{u}_{in} \\ \hat{i}_o \end{bmatrix} = \begin{bmatrix} 0 & 1 \\ 1 & 0 \end{bmatrix} \begin{bmatrix} \hat{i}_L \\ \hat{u}_C \end{bmatrix} + \begin{bmatrix} 0 & 0 & 0 \\ 0 & 0 & 0 \end{bmatrix} \begin{bmatrix} \hat{i}_{in} \\ \hat{u}_o \\ \hat{d} \end{bmatrix}. \tag{2.8}$$

This corresponds to the well-known state-space representation presented in (2.9). The output variables \mathbf{Y} can be solved as a function of the input variables \mathbf{U} by transforming equations to Laplace domain and solving the mappings from the input variables to the output variables, which gives (2.10).

$$\begin{aligned}
\dot{\mathbf{x}} &= \mathbf{Ax} + \mathbf{Bu} \\
\mathbf{y} &= \mathbf{Cx} + \mathbf{Du}
\end{aligned} \tag{2.9}$$

$$\mathbf{Y} = \mathbf{C} [(\mathbf{sI} - \mathbf{A})^{-1}\mathbf{B} + \mathbf{D}] \mathbf{U} = \mathbf{G}_H \mathbf{U} \tag{2.10}$$

The obtained matrix \mathbf{G}_H contains transfer functions describing the dynamics of the converter at open loop. Transfer function set for the example converter is shown in (2.11).

$$\begin{bmatrix} \hat{u}_{in} \\ \hat{i}_o \end{bmatrix} = \begin{bmatrix} Z_{in-o} & T_{oi-o} & G_{ci-o} \\ G_{io-o} & -Y_{o-o} & G_{co-o} \end{bmatrix} \begin{bmatrix} \hat{i}_{in} \\ \hat{u}_o \\ \hat{d} \end{bmatrix} \tag{2.11}$$

According to (2.11), the converter can be modeled as a linear two port system [18]. The input port is modeled as a series connection of two dependent voltage sources and an input impedance, while the output port is modeled as a parallel connection of two dependent current sources and an output admittance. The minus sign in the second row of (2.11) is required since the current flowing out of the converter is defined positive. The hat over the variables denote that they represent small-signal variations around the steady-state operating point. Resulting two-port model is given in Fig. 2.4.

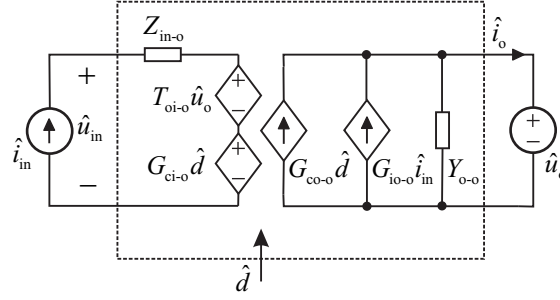


Figure 2.4: Linear small-signal model of a current-fed converter.

Control block diagram is another useful representation which can be derived from (2.11). From the control block diagram, closed-loop transfer functions can be easily solved and control loops identified to help with the control system design. Open-loop block diagrams for input and output dynamics of the example converter are shown in Fig. 2.5.

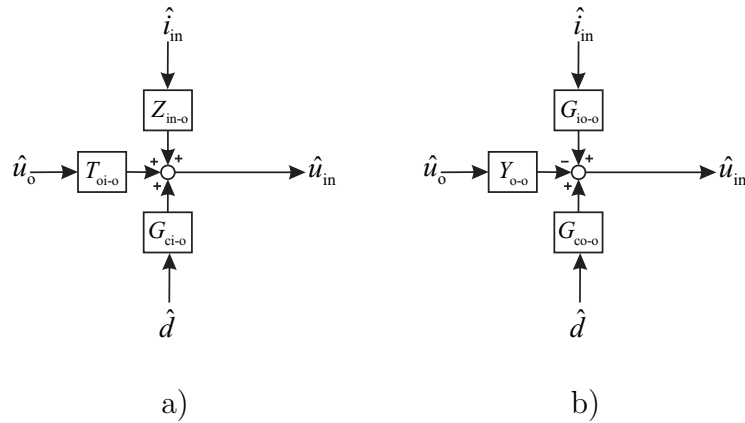


Figure 2.5: Control block diagrams at open loop for a) input and b) output dynamics.

2.4 Source and load effects

Until now, only ideal source and load systems have been considered. In fact, the real sources have finite internal impedances. The effects of nonideal source and load can be included with the help of the two-port model. For source interactions the internal

impedance of a current source is taken into account and the source is modeled as a Norton equivalent circuit as depicted in Fig. 2.6. The current flowing into the power stage is different from the ideal case, since part of it flows through the branch containing source admittance Y_S .

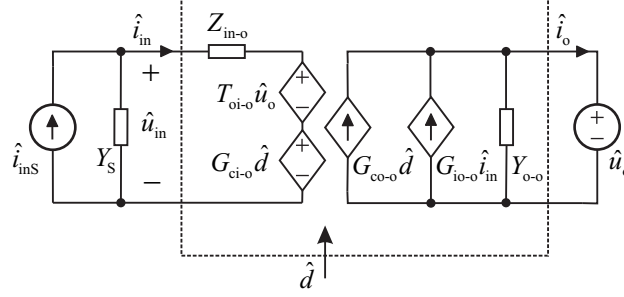


Figure 2.6: Linear small-signal model with a non-ideal source.

According to KVL, the input current of the power stage can be solved from Fig. 2.6, by first transforming the non-ideal source to a Thevenin equivalent circuit. This results in a new presentation for the input current (2.12), which can be inserted to the matrix (2.11). The resulting source-affected input- and output dynamics are as shown in (2.13).

$$\hat{i}_{in} = \frac{1}{1 + Z_{in-o}Y_S} \hat{i}_{inS} - \frac{T_{oi-o}Y_S}{1 + Z_{in-o}Y_S} \hat{u}_o - \frac{G_{ci-o}Y_S}{1 + Z_{in-o}Y_S} \hat{d} \quad (2.12)$$

$$\begin{bmatrix} \hat{u}_{in} \\ \hat{i}_o \end{bmatrix} = \begin{bmatrix} \frac{Z_{in-o}}{1 + Y_S Z_{in-o}} & \frac{T_{oi-o}}{1 + Y_S Z_{in-o}} & \frac{G_{ci-o}}{1 + Y_S Z_{in-o}} \\ \frac{G_{io-o}}{1 + Y_S Z_{in-o}} & -\frac{1 + Y_S Z_{in-oco}}{1 + Y_S Z_{in-o}} Y_{o-o} & \frac{1 + Y_S Z_{in-\infty}}{1 + Y_S Z_{in-o}} G_{co-o} \end{bmatrix} \begin{bmatrix} \hat{i}_{inS} \\ \hat{u}_o \\ \hat{d} \end{bmatrix} \quad (2.13)$$

where,

$$Z_{in-oco} = Z_{in-o} + \frac{G_{io-o}T_{oi-o}}{Y_{o-o}}$$

and

$$Z_{in-\infty} = Z_{in-o} - \frac{G_{io-o}G_{ci-o}}{G_{co-o}}$$

are open-circuit and ideal input impedances.

The effect of a non-ideal load can be considered by including the internal impedance of the load voltage to the two-port model as shown in Fig. 2.7. The load is transformed to a Norton equivalent circuit and the resulting power stage output voltage (2.14) is then inserted to (2.11). The load-affected transfer functions are presented in (2.15).

3. SPACE-VECTOR THEORY

Space-vector theory was developed originally as a tool to analyze transient states in electrical machines. A three-phase system can be described with a complex time-dependent space-vector and its zero component. The space-vector of any three-phase system and its zero component are defined as in (3.1) and (3.2) [19].

$$\underline{x}(t) = \frac{2}{3} (x_a(t) + \underline{a}x_b(t) + \underline{a}^2x_c(t)) \quad (3.1)$$

$$x_z(t) = \frac{1}{3} (x_a(t) + x_b(t) + x_c(t)), \quad (3.2)$$

where

$$\underline{a} = e^{j2\pi/3} = -\frac{1}{2} + j\frac{\sqrt{3}}{2} \quad (3.3)$$

The coefficient $2/3$ produces a space-vector which has the same length as the amplitude of a phase-variable in a balanced three-phase system. The power of the transformed system is as shown in (3.4) [20]. This type of transformation is also called an amplitude invariant transformation.

$$p = \frac{3}{2} \text{Re} \{ \underline{u} \underline{i}^* \} \quad (3.4)$$

Another widely used transformation is the power invariant version, in which the factor $2/3$ is replaced with its square root $\sqrt{2/3}$. In the power invariant version, the power of the three-phase system is the voltage space-vector multiplied with the current space-vector complex conjugate. In this type of transformation, the length of the space-vector is not anymore equal to the phase-variable amplitude. The power invariant space-vector transformation will not be discussed here, because in this work the amplitude invariant version is used.

Applying space-vector transformation (3.1) to a three-phase system results in a vector consisting of two components in a stationary α - β -reference frame, in which the vector rotates at the fundamental grid frequency ω_s as shown in Fig. 3.1. A symmetrical and balanced three-phase system has no zero component.

Transformation of three-phase variables to a stationary reference frame can be done directly by using Clarke's transformation matrix as presented in (3.5).

$$\begin{bmatrix} x_\alpha \\ x_\beta \\ x_z \end{bmatrix} = \frac{2}{3} \begin{bmatrix} 1 & -1/2 & -1/2 \\ 0 & \sqrt{3}/2 & -\sqrt{3}/2 \\ 1/2 & 1/2 & 1/2 \end{bmatrix} \begin{bmatrix} x_a \\ x_b \\ x_c \end{bmatrix} \quad (3.5)$$

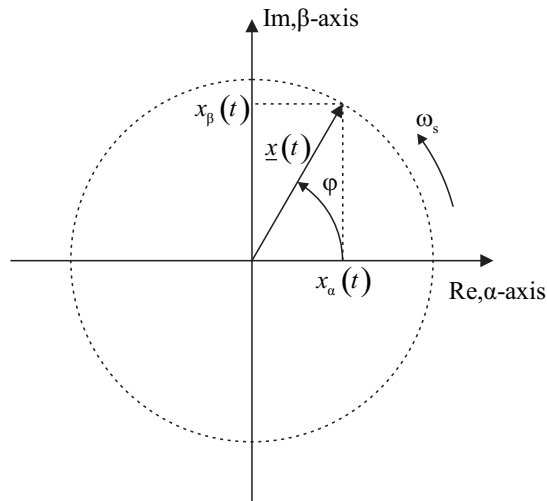


Figure 3.1: Space-vector in a stationary reference frame.

The space-vector in a stationary frame can be transformed back to three-phase variables, if the zero component is known, by using inverse Clarke's transformation matrix (3.6).

$$\begin{bmatrix} x_a \\ x_b \\ x_c \end{bmatrix} = \begin{bmatrix} 1 & -0 & 1 \\ -1/2 & \sqrt{3}/2 & 1 \\ -1/2 & -\sqrt{3}/2 & 1 \end{bmatrix} \begin{bmatrix} x_\alpha \\ x_\beta \\ x_z \end{bmatrix} \quad (3.6)$$

As previously mentioned, the Clarke's transformation produces a space-vector which rotates in a stationary reference frame with angular frequency ω_s . The space-vector can be transformed to a synchronous reference frame which rotates at the same frequency as the space-vector by applying (3.7).

$$\underline{x}^s = |\underline{x}| e^{j(\varphi - \theta_s)} = |\underline{x}| e^{j\varphi} e^{-j\theta_s} = \underline{x} e^{-j\theta_s} = \underline{x} e^{-j\omega_s t}, \quad (3.7)$$

where \underline{x} is the original space-vector in the stationary reference frame and \underline{x}^s is the space-vector in the synchronous reference frame. The resulting space-vector has only dc-valued components, if the frame is rotating with grid frequency and symmetrical grid voltages are assumed. The synchronous reference frame is illustrated in Fig. 3.2. The real axis of the rotating frame is called direct (d) and the imaginary axis is called quadrature (q) axis.

Backward transformation from synchronous frame to stationary frame can be done as in (3.8).

$$\underline{x} = \underline{x}^s e^{j\omega_s t}, \quad (3.8)$$

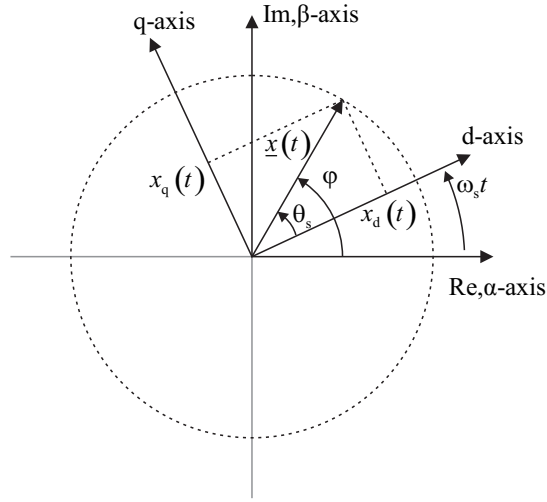


Figure 3.2: Space-vector in a synchronous reference frame.

Transformation from variables in stationary frame to synchronous frame can be given in a matrix form as presented in (3.9). The inverse transformation transforms the variables back to the stationary frame and is as shown in (3.10).

$$\begin{bmatrix} x_d \\ x_q \\ x_z \end{bmatrix} = \begin{bmatrix} \cos\theta_s & \sin\theta_s & 0 \\ -\sin\theta_s & \cos\theta_s & 0 \\ 0 & 0 & 1 \end{bmatrix} \begin{bmatrix} x_\alpha \\ x_\beta \\ x_z \end{bmatrix} \quad (3.9)$$

$$\begin{bmatrix} x_\alpha \\ x_\beta \\ x_z \end{bmatrix} = \begin{bmatrix} \cos\theta_s & -\sin\theta_s & 0 \\ \sin\theta_s & \cos\theta_s & 0 \\ 0 & 0 & 1 \end{bmatrix} \begin{bmatrix} x_d \\ x_q \\ x_z \end{bmatrix} \quad (3.10)$$

Space-vector transformation can be done directly from the three-phase variables to synchronous frame with Park's transformation matrix (3.11). The inverse transformation back to three-phase variables can be done with (3.12).

$$\begin{bmatrix} x_d \\ x_q \\ x_z \end{bmatrix} = \frac{2}{3} \begin{bmatrix} \cos\theta_s & \cos(\theta_s - 2\pi/3) & \cos(\theta_s - 4\pi/3) \\ -\sin\theta_s & -\sin(\theta_s - 2\pi/3) & -\sin(\theta_s - 4\pi/3) \\ 1/2 & 1/2 & 1/2 \end{bmatrix} \begin{bmatrix} x_a \\ x_b \\ x_c \end{bmatrix} \quad (3.11)$$

$$\begin{bmatrix} x_a \\ x_b \\ x_c \end{bmatrix} = \begin{bmatrix} \cos\theta_s & -\sin\theta_s & 1 \\ \cos(\theta_s - 2\pi/3) & -\sin(\theta_s - 2\pi/3) & 1 \\ \cos(\theta_s - 4\pi/3) & -\sin(\theta_s - 4\pi/3) & 1 \end{bmatrix} \begin{bmatrix} x_d \\ x_q \\ x_z \end{bmatrix} \quad (3.12)$$

4. SMALL-SIGNAL MODELLING OF THREE-PHASE INVERTERS

Small-signal modeling is straightforward in the case of dc-dc converters. Modeling procedure requires that the small-signal model is linearized at a steady-state operating point. However, the voltages and currents on the ac-side of a three-phase inverter are sinusoidal and therefore a steady-state operating point does not exist. Thus conventional small-signal modeling presented in Chapter 2 cannot be directly applied.

There is a great deal of articles dealing with inverter modeling in the literature. The most widely reported modeling procedure is to perform the analysis in the synchronous reference frame [21]. Transforming the symmetrical and balanced three-phase variables into the synchronous reference frame results in a presentation where only dc-valued variables are present.

A small-signal model for a two-level three-phase inverter is derived in this chapter based on the small-signal modeling presented in Chapter 2 and the space-vector theory discussed in Chapter 3.

4.1 Three-phase inverter

A conventional two-level three-phase inverter, usually called as a voltage sourced inverter (VSI) in the literature, is depicted in Fig 4.1.

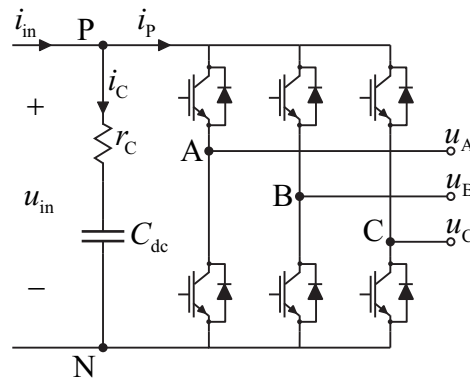


Figure 4.1: Voltage source inverter as usually depicted in the literature.

The inverter produces its grid side voltages by switching between different switching states. Each terminal (A,B,C) can be connected to either the positive or negative dc-rail. Switching states are restricted to eight different cases to avoid short circuiting the dc-side capacitor, i.e. both switches on the same inverter leg can never be turned

on simultaneously. Each switching state can be presented in a space-vector form by applying definitions (3.1) and (3.2). The allowed switching vectors are shown in Table 4.1, where '+' denotes that the output terminal is connected to the positive and '-' to the negative dc-rail. Zero output voltage vector can be formed by connecting all three phases to the same potential, either negative or positive dc-rail. Resulting switching vectors without the zero components are depicted in Fig. 4.2.

Table 4.1: Switching vectors of a three-phase two-level inverter.

Switching state	u_A	u_B	u_C	u_α/u_{in}	u_β/u_{in}
u_{0-}	-	-	-	0	0
u_1	+	-	-	$+2/3$	0
u_2	+	+	-	$+1/3$	$+\sqrt{3}/3$
u_3	-	+	-	$-1/3$	$+\sqrt{3}/3$
u_4	-	+	+	$-2/3$	0
u_5	-	-	+	$-1/3$	$-\sqrt{3}/3$
u_6	+	-	+	$+1/3$	$-\sqrt{3}/3$
u_{0+}	+	+	+	0	0

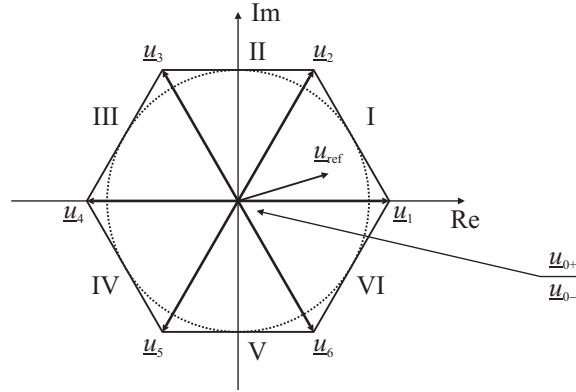


Figure 4.2: Space vectors produced by a two-level three-phase inverter.

Two most used modulation methods for three-phase two-level inverters are space-vector and carrier-based pulse-width modulation. In space-vector modulation, the three-phase reference voltages are first transformed into a single complex valued space-vector, which is shown in Fig 4.2 and denoted by \underline{u}_{ref} . The output-voltage vector is produced by averaging the switching times of the two nearest switching vectors and both zero vectors over one switching period. On the average, the grid-side voltages follow the space-vector transformed reference voltage.

In case of Fig. 4.2, the resulting output voltage vector of the inverter would be

$$\underline{u}_{ref} \approx \underline{u}_o = d_1 \underline{u}_1 + d_2 \underline{u}_2 + \frac{d_0}{2} \underline{u}_{0+} + \frac{d_0}{2} \underline{u}_{0-}, \quad (4.1)$$

where d_1 is the duty ratio for the switch-state \underline{u}_1 and d_2 for the \underline{u}_2 . The remaining time is divided between the two zero states. Their total duty ratio is denoted by d_0 .

In the carrier-based PWM method, three sinusoidal reference voltages phase-shifted by 120° [22], are compared with a sawtooth waveform as shown in Fig. 4.3. When the reference is greater than sawtooth, the phase is connected to the positive dc-rail and vice versa. The frequency of the sawtooth waveform is in reality much higher than in the figure, several kilohertz in real applications. The voltages at the inverter output terminals follow the reference voltages on average. The higher the sawtooth frequency, the smaller is the current ripple and smaller inductors can be used. In this thesis the PWM method for the three-phase inverter is assumed.

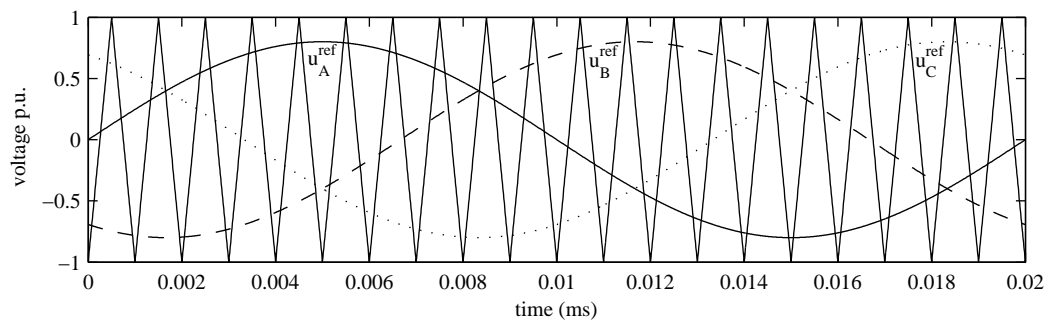


Figure 4.3: Voltage waveforms related to carrier-based pulse-width modulation method for a three-phase two-level inverter.

4.2 Control of a three-phase inverter

A cascaded control structure is usually implemented in photovoltaic interfacing converters [23]. Some approaches use measured input and output powers to calculate the output current reference, such as [24]. Maximum power point tracking (MPPT) is usually realized by controlling the generator voltage rather than the current. This is because the voltage changes slowly along with the ambient temperature but the current can change rapidly when irradiation changes [25]. The control system can be implemented in a synchronous reference frame, which rotates with the same angular frequency as the grid fundamental component. In the synchronous reference frame, sinusoidal three-phase signals become dc-valued variables and errors can be compensated using simple PI control structures. A control system implemented in a synchronous reference frame is depicted in Fig. 4.4. q-component of the reference current is usually set to zero to achieve unity power factor.

The outer loop is responsible for the input voltage control which is necessary in order to operate the panel at its maximum power point (MPP). The inner loop controls the output current to be in phase with the grid voltage to reach unity power factor. Output voltage feedforward and decoupling terms are usually included to compensate the dependence of d- and q-variables of each other [26] but are omitted in this thesis. Phase-locked loop (PLL) is used to extract the phase angle from the grid voltage which

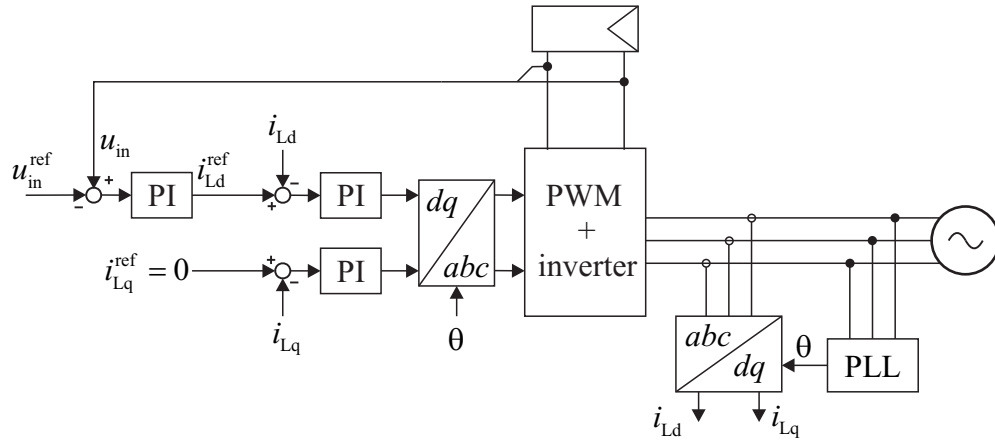


Figure 4.4: Control system implemented in the synchronous reference frame using PI controllers.

is needed for the dq-transformation. Modulation can be implemented by transforming the reference vector from synchronous frame to the three-phase variables and using conventional PWM, or it can be fed directly to a space vector modulator (SVM PWM).

It has to be noted that the control signal of the voltage controller must be inverted by multiplying it with -1. This is equivalent to connecting the input voltage reference value to the negative side and measurement to the positive side of the summer, as depicted in Fig. 4.4. It can be understood by considering the input capacitor in Fig. 4.1 when the input is a current source, such as a PV panel: the voltage of the capacitor depends on the current flowing into it according to basic circuit analysis. Thus increasing the output current reference leads to reduction of the capacitor voltage, because the input current is determined by the panel. On the other hand, reducing the output current reference makes more of the input current flow into the capacitor and causes its voltage to rise.

4.3 Averaged model in the synchronous reference frame

The power stage of a conventional three-phase inverter usually adopted in photovoltaic applications is depicted in Fig 4.5. The input terminal is connected to a current source due to physical nature of a PV generator. The output terminals are connected to an ideal three-phase grid modeled with three ac-voltage sources, phase-shifted by 120° .

Some current filtering is needed to comply with the grid current requirements. There exists a great deal of different standards for grid-connected PV systems. To date no unified standard exist but probably the most used standard is IEEE 929-2000 [27]. Two most used techniques for current filtering are to implement sufficient amount of inductance on the grid side or use an LCL-filter. In this thesis a balanced three-phase inductor is used as a grid current filter but the modeling can be done also when an LCL-filter is used.

The average voltage in respect to dc-side negative rail of any output terminal de-

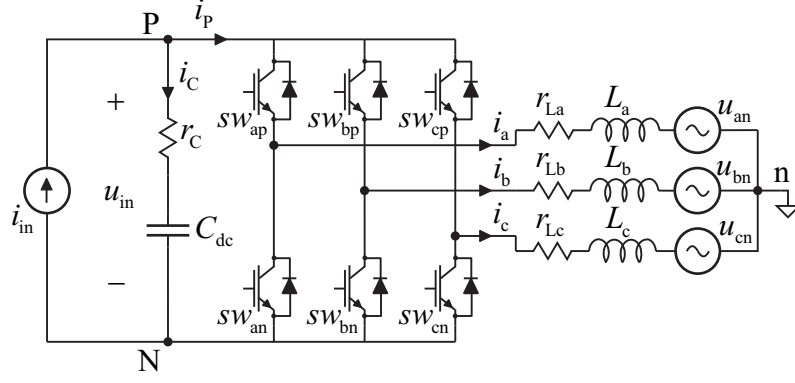


Figure 4.5: Power stage of a three-phase two-level inverter.

depends on the duty ratio of the upper switch d_i , where $i = A, B, C$. Equations for average voltages over the inductors (4.2)-(4.4) are obtained by using KVL and taking into account the inverter common-mode voltage u_{nN} .

$$\langle u_{La} \rangle = d_A \langle u_{in} \rangle - R_1 \langle i_{La} \rangle - \langle u_{an} \rangle - \langle u_{nN} \rangle \quad (4.2)$$

$$\langle u_{Lb} \rangle = d_B \langle u_{in} \rangle - R_1 \langle i_{Lb} \rangle - \langle u_{bn} \rangle - \langle u_{nN} \rangle \quad (4.3)$$

$$\langle u_{Lc} \rangle = d_C \langle u_{in} \rangle - R_1 \langle i_{Lc} \rangle - \langle u_{cn} \rangle - \langle u_{nN} \rangle, \quad (4.4)$$

where R_1 is the total resistance along the current path. The switches are assumed to have equal parasitic resistances. The same assumption is made for the grid-side inductors.

According to KCL, the dc-side capacitor is supplied by the current flowing from the input source and loaded by the current flowing to the output terminals depending on the switching state. The average current flowing to the grid i_P depends on the duty cycle of the upper switches and is the sum of phase currents. Dc-side voltage is the sum of capacitor voltage and the voltage over its parasitic resistance r_C . Resulting equations for capacitor current and dc-side voltage are presented in (4.5) and (4.6).

$$\langle i_C \rangle = -d_A \langle i_{La} \rangle - d_B \langle i_{Lb} \rangle - d_C \langle i_{Lc} \rangle + \langle i_{in} \rangle \quad (4.5)$$

$$\langle u_{in} \rangle = -d_A r_C \langle i_{La} \rangle - d_B r_C \langle i_{Lb} \rangle - d_C r_C \langle i_{Lc} \rangle + \langle u_C \rangle + r_C \langle i_{in} \rangle \quad (4.6)$$

Inductor voltage equation (4.2) can be multiplied by $\frac{2}{3}e^{j0}$, (4.3) by $\frac{2}{3}e^{j\frac{2\pi}{3}}$ and (4.4) by $\frac{2}{3}e^{j\frac{4\pi}{3}}$. Summing these three equations together results in an equation that is equivalent to a space-vector representation of the inductor voltages (4.7).

$$\langle \underline{u}_L \rangle = \underline{d} \langle \underline{u}_{in} \rangle - R_1 \langle \underline{i}_L \rangle - \langle \underline{u}_o \rangle, \quad (4.7)$$

where

$$\underline{d} = \frac{2}{3} \left(d_A e^{j0} + d_B e^{j\frac{2\pi}{3}} + d_C e^{j\frac{4\pi}{3}} \right), \quad (4.8)$$

$$\langle i_L \rangle = \frac{2}{3} \left(\langle i_{La} \rangle e^{j0} + \langle i_{Lb} \rangle e^{j\frac{2\pi}{3}} + \langle i_{Lc} \rangle e^{j\frac{4\pi}{3}} \right), \quad (4.9)$$

$$\langle u_o \rangle = \frac{2}{3} \left(\langle u_{an} \rangle e^{j0} + \langle u_{bn} \rangle e^{j\frac{2\pi}{3}} + \langle u_{cn} \rangle e^{j\frac{4\pi}{3}} \right). \quad (4.10)$$

The common-mode voltage disappears, since the averaged duty ratios are continuous and balanced and $\frac{2}{3} \left(e^{j0} + e^{j\frac{2\pi}{3}} + e^{j\frac{4\pi}{3}} \right)$ equals zero. Equation (4.7) can be transformed to the synchronous reference frame by using (3.8) as done in (4.11).

$$\begin{aligned} \frac{d \left(\langle i_L^s \rangle e^{j\omega_s t} \right)}{dt} &= \frac{1}{L} \underline{d}^s \langle u_{in} \rangle e^{j\omega_s t} - \frac{R_1}{L} \langle i_L^s \rangle e^{j\omega_s t} - \frac{1}{L} \langle u_o^s \rangle e^{j\omega_s t} \\ \frac{d \langle i_L^s \rangle}{dt} &= - \left(j\omega_s + \frac{R_1}{L} \right) \langle i_L^s \rangle + \frac{1}{L} \underline{d}^s \langle u_{in} \rangle - \frac{1}{L} \langle u_o^s \rangle, \end{aligned} \quad (4.11)$$

where superscript s denotes that the variable is in the synchronous reference frame. The term $-j\omega_s \langle i_L^s \rangle$, which appears in the coordinate transformation, accounts for the cross-coupling between the d- and q- components of the current.

The capacitor current d- and q-components can be solved by using the inverse Clark's transformation (3.6) for all three phase currents and duty ratios in (4.5) and transforming the obtained results to the synchronous reference frame as done in (4.12).

$$\begin{aligned} \langle i_C \rangle &= -d_A \langle i_{La} \rangle - d_B \langle i_{Lb} \rangle - d_C \langle i_{Lc} \rangle + \langle i_{in} \rangle \\ &= -\frac{3}{2} \text{Re} \left(\underline{d} \langle i_L^* \rangle \right) + \langle i_{in} \rangle \\ &= -\frac{3}{2} \text{Re} \left(\underline{d}^s e^{j\omega_s t} \left(\langle i_L^s \rangle e^{j\omega_s t} \right)^* \right) + \langle i_{in} \rangle \\ &= -\frac{3}{2} \text{Re} \left(\underline{d}^s e^{j\omega_s t} \langle i_L^{s*} \rangle e^{-j\omega_s t} \right) + \langle i_{in} \rangle \\ &= -\frac{3}{2} \text{Re} \left(\underline{d}^s \langle i_L^{s*} \rangle \right) + \langle i_{in} \rangle \\ &= -\frac{3}{2} (d_d \langle i_{Ld} \rangle + d_q \langle i_{Lq} \rangle) + \langle i_{in} \rangle \end{aligned} \quad (4.12)$$

By substituting (4.12) to (4.6), the input voltage can be presented in terms of dc-quantities and components in the synchronous reference frame as shown in (4.13).

$$\langle u_{in} \rangle = -\frac{3}{2} r_C d_d \langle i_{Ld} \rangle - \frac{3}{2} r_C d_q \langle i_{Lq} \rangle + r_C \langle i_{in} \rangle + \langle u_C \rangle \quad (4.13)$$

Substituting (4.13) to the inductor current differential equation (4.11) and dividing the current to d- (4.14) and q-components (4.15), results in a representation of derivatives of the current components, which contain only dc-quantities or components in the synchronous reference frame.

$$\begin{aligned}
\frac{d \langle i_{Ld} \rangle}{dt} = & - \left(\frac{R_1}{L} + \frac{3r_C}{2L} d_d^2 \right) \langle i_{Ld} \rangle + \left(\omega_s - \frac{3r_C}{2L} d_d d_q \right) \langle i_{Lq} \rangle \\
& + \frac{r_C}{L} d_d \langle i_{in} \rangle + \frac{1}{L} d_d \langle u_C \rangle - \frac{1}{L} \langle u_{od} \rangle
\end{aligned} \tag{4.14}$$

$$\begin{aligned}
\frac{d \langle i_{Lq} \rangle}{dt} = & - \left(\omega_s + \frac{3r_C}{2L} d_d d_q \right) \langle i_{Ld} \rangle - \left(\frac{R_1}{L} + \frac{3r_C}{2L} d_q^2 \right) \langle i_{Lq} \rangle \\
& + \frac{r_C}{L} d_q \langle i_{in} \rangle + \frac{1}{L} d_q \langle u_C \rangle - \frac{1}{L} \langle u_{oq} \rangle
\end{aligned} \tag{4.15}$$

The derivative of the capacitor voltage equals the current i_C flowing to the capacitor, as in (4.12), divided by its capacitance C . Derivative of the capacitor voltage is as shown in (4.16).

$$\frac{d \langle u_C \rangle}{dt} = - \frac{3}{2C} d_d \langle i_{Ld} \rangle - \frac{3}{2C} d_q \langle i_{Lq} \rangle + \frac{1}{C} \langle i_{in} \rangle \tag{4.16}$$

Equations (4.13)-(4.16) represent the averaged model of the inverter, where the grid side is transformed to the synchronous reference frame. The steady-state operation point can now be solved by setting derivative terms to zero and replacing averaged values with their corresponding steady-state values as explained in Chapter 3. The grid current q-component steady-state value is assumed to be zero in the following analysis, because usually unity power factor operation is desired. Thus, only real power is transferred to the grid. The grid voltage q-component steady-state value is also zero because an ideal three-phase grid is assumed.

The steady-state value of the output current d-component can be solved from (4.16) by

$$I_{Ld} = \frac{2I_{in}}{3D_d}. \tag{4.17}$$

The current d-component steady-state value can be substituted to (4.13) and the steady-state value for the capacitor voltage can be given by (4.18)

$$U_C = U_{in}. \tag{4.18}$$

Substituting (4.17) and (4.18) to (4.14) yields a second order polynomial for the d-component of the duty ratio as

$$U_{in} D_d^2 - U_{od} D_d - \frac{2R_1 I_{in}}{3} = 0, \tag{4.19}$$

from which the steady-state value of the duty ratio d-component can be solved by

$$D_d = \frac{U_{od} + \sqrt{(-U_{od})^2 + 4U_{in} \left(\frac{2R_1 I_{in}}{3} \right)}}{2U_{in}}. \quad (4.20)$$

Similarly, the q-component of the duty ratio can be solved from (4.15) by

$$D_q = \frac{2\omega_s L I_{in}}{3D_d U_{in}}. \quad (4.21)$$

4.4 Linearized state-space model in the synchronous reference frame

Equations (4.13),(4.14),(4.15) and (4.16) represent the averaged model of the converter. This nonlinear model can be linearized at a desired operation point by taking first order derivatives in respect to input and state variables and denoting all variables with their steady-state values as presented above and denoting $I_{Lq} = 0$. The resulting linearized small-signal model is as shown in (4.22) - (4.27).

$$\begin{aligned} \frac{d\hat{i}_{Ld}}{dt} = & - \left(\frac{R_1}{L} + \frac{3r_C}{2L} D_d^2 \right) \hat{i}_{Ld} + \left(\omega_s - \frac{r_C \omega_s I_{in}}{U_{in}} \right) \hat{i}_{Lq} + \frac{D_d}{L} \hat{u}_C \\ & + \frac{r_C D_d}{L} \hat{i}_{in} - \frac{1}{L} \hat{u}_{od} + \frac{U_{in} - r_C I_{in}}{L} \hat{d}_d \end{aligned} \quad (4.22)$$

$$\begin{aligned} \frac{d\hat{i}_{Lq}}{dt} = & - \left(\omega_s + \frac{r_C \omega_s I_{in}}{U_{in}} \right) \hat{i}_{Ld} - \left(\frac{R_1}{L} + \frac{3r_C}{2L} D_q^2 \right) \hat{i}_{Lq} + \frac{D_q}{L} \hat{u}_C \\ & + \frac{r_C D_q}{L} \hat{i}_{in} - \frac{1}{L} \hat{u}_{oq} - \frac{r_C D_q I_{in}}{D_d L} \hat{d}_d + \frac{U_{in}}{L} \hat{d}_q \end{aligned} \quad (4.23)$$

$$\frac{d\hat{u}_C}{dt} = -\frac{3D_d}{2C} \hat{i}_{Ld} - \frac{3D_q}{2C} \hat{i}_{Lq} + \frac{1}{C} \hat{i}_{in} - \frac{I_{in}}{D_d C} \hat{d}_d \quad (4.24)$$

$$\hat{u}_{in} = -\frac{3D_d r_C}{2} \hat{i}_{Ld} - \frac{3D_q r_C}{2} \hat{i}_{Lq} + \hat{u}_C + r_C \hat{i}_{in} - \frac{r_C I_{in}}{D_d} \hat{d}_d \quad (4.25)$$

$$\hat{i}_{od} = \hat{i}_{Ld} \quad (4.26)$$

$$\hat{i}_{oq} = \hat{i}_{Lq} \quad (4.27)$$

The linearized state-space model can be presented in matrix form yielding (4.28) and (4.29).

$$\begin{aligned}
\begin{bmatrix} \frac{d\hat{i}_{Ld}}{dt} \\ \frac{d\hat{i}_{Lq}}{dt} \\ \frac{d\hat{u}_C}{dt} \end{bmatrix} &= \begin{bmatrix} -\left(\frac{R_1}{L} + \frac{3r_C}{2L}D_d^2\right) & \left(\omega_s - \frac{r_C\omega_s I_{in}}{U_{in}}\right) & \frac{D_d}{L} \\ -\left(\omega_s + \frac{r_C\omega_s I_{in}}{U_{in}}\right) & -\left(\frac{R_1}{L} + \frac{3r_C}{2L}D_q^2\right) & \frac{D_q}{L} \\ -\frac{3D_d}{2C} & -\frac{3D_q}{2C} & 0 \end{bmatrix} \begin{bmatrix} \hat{i}_{Ld} \\ \hat{i}_{Lq} \\ \hat{u}_C \end{bmatrix} \\
&+ \begin{bmatrix} \frac{r_C D_d}{L} & -\frac{1}{L} & 0 & \frac{U_{in}-r_C I_{in}}{L} & 0 \\ \frac{r_C D_q}{L} & 0 & -\frac{1}{L} & -\frac{r_C D_q I_{in}}{D_d L} & \frac{U_{in}}{L} \\ \frac{1}{C} & 0 & 0 & -\frac{I_{in}}{D_d C} & 0 \end{bmatrix} \begin{bmatrix} \hat{i}_{in} \\ \hat{u}_{od} \\ \hat{u}_{oq} \\ \hat{d}_d \\ \hat{d}_q \end{bmatrix} \quad (4.28)
\end{aligned}$$

$$\begin{aligned}
\begin{bmatrix} \hat{u}_{in} \\ \hat{i}_{od} \\ \hat{i}_{oq} \end{bmatrix} &= \begin{bmatrix} -\frac{3D_d r_C}{2} & -\frac{3D_q r_C}{2} & 1 \\ 1 & 0 & 0 \\ 0 & 1 & 0 \end{bmatrix} \begin{bmatrix} \hat{i}_{Ld} \\ \hat{i}_{Lq} \\ \hat{u}_C \end{bmatrix} \\
&+ \begin{bmatrix} r_C & 0 & 0 & -\frac{r_C I_{in}}{D_d} & 0 \\ 0 & 0 & 0 & 0 & 0 \\ 0 & 0 & 0 & 0 & 0 \end{bmatrix} \begin{bmatrix} \hat{i}_{in} \\ \hat{u}_{od} \\ \hat{u}_{oq} \\ \hat{d}_d \\ \hat{d}_q \end{bmatrix} \quad (4.29)
\end{aligned}$$

The obtained matrix presentation is next transformed to Laplace domain and mappings from input variables to output variables are solved according to (2.10). This gives a matrix containing small-signal transfer functions that describe the dynamics of the inverter input, d and q-channels (4.30) at open loop.

$$\begin{bmatrix} \hat{u}_{in} \\ \hat{i}_{od} \\ \hat{i}_{oq} \end{bmatrix} = \begin{bmatrix} Z_{in} & T_{oi-d} & T_{oi-q} & G_{ci-d} & G_{ci-q} \\ G_{io-d} & -Y_{o-d} & G_{cr-qd} & G_{co-d} & G_{co-qd} \\ G_{io-q} & G_{cr-dq} & -Y_{o-q} & G_{co-dq} & G_{co-q} \end{bmatrix} \begin{bmatrix} \hat{i}_{in} \\ \hat{u}_{od} \\ \hat{u}_{oq} \\ \hat{d}_d \\ \hat{d}_q \end{bmatrix} \quad (4.30)$$

The transfer functions for the three-phase two-level inverter at open loop when

parasitic components are omitted, are presented in (4.31) - (4.45).

$$\Delta Z_{\text{in}} = \frac{1}{C} (s^2 + \omega_s^2) \quad (4.31)$$

$$\Delta T_{\text{oi-d}} = \frac{3D_d}{2CL} \left(s - \frac{D_q}{D_d} \omega_s \right) \quad (4.32)$$

$$\Delta T_{\text{oi-q}} = \frac{3D_q}{2CL} \left(s + \frac{D_d}{D_q} \omega_s \right) \quad (4.33)$$

$$\Delta G_{\text{ci-d}} = -\frac{I_{\text{in}}}{D_d C} s \left(s + \frac{3D_d^2 U_{\text{in}}}{2LI_{\text{in}}} \right) \quad (4.34)$$

$$\Delta G_{\text{ci-q}} = -\frac{\omega_s I_{\text{in}}}{D_d C} \left(s + \frac{3D_d^2 U_{\text{in}}}{2LI_{\text{in}}} \right) \quad (4.35)$$

$$\Delta G_{\text{io-d}} = \frac{D_d}{LC} \left(s + \frac{D_q}{D_d} \omega_s \right) \quad (4.36)$$

$$\Delta Y_{\text{o-d}} = \frac{1}{L} \left(s^2 + \frac{3D_q^2}{2LC} \right) \quad (4.37)$$

$$\Delta G_{\text{cr-qd}} = -\frac{\omega_s}{L} \left(s - \frac{3D_d D_q}{2\omega_s LC} \right) \quad (4.38)$$

$$\Delta G_{\text{co-d}} = \frac{U_{\text{in}}}{L} s \left(s - \frac{I_{\text{in}}}{CU_{\text{in}}} \right) \quad (4.39)$$

$$\Delta G_{\text{co-qd}} = \frac{U_{\text{in}} \omega_s}{L} \left(s - \frac{I_{\text{in}}}{CU_{\text{in}}} \right) \quad (4.40)$$

$$\Delta G_{\text{io-q}} = \frac{D_q}{LC} \left(s - \frac{D_d}{D_q} \omega_s \right) \quad (4.41)$$

$$\Delta G_{\text{cr-dq}} = \frac{\omega_s}{L} \left(s + \frac{I_{\text{in}}}{CU_{\text{in}}} \right) \quad (4.42)$$

$$\Delta Y_{\text{o-q}} = \frac{1}{L} \left(s^2 + \frac{3D_d^2}{2LC} \right) \quad (4.43)$$

$$\Delta G_{\text{co-dq}} = -\frac{1}{L} s \left(U_{\text{in}} \omega_s + \frac{D_q I_{\text{in}}}{D_d C} \right) \quad (4.44)$$

$$\Delta G_{\text{co-q}} = \frac{U_{\text{in}}}{L} \left(s^2 + \frac{3D_d^2}{2LC} \right) \quad (4.45)$$

$$\Delta = s \left(s^2 + \frac{3(D_d^2 + D_q^2)}{2LC} + \omega_s^2 \right) \quad (4.46)$$

From (4.30), a linear network model can be constructed as depicted in Fig. 4.6. The system has two output channels, which are coupled by transfer functions $G_{\text{cr-qd}}$, $G_{\text{co-qd}}$, $G_{\text{cr-dq}}$ and $G_{\text{co-dq}}$.

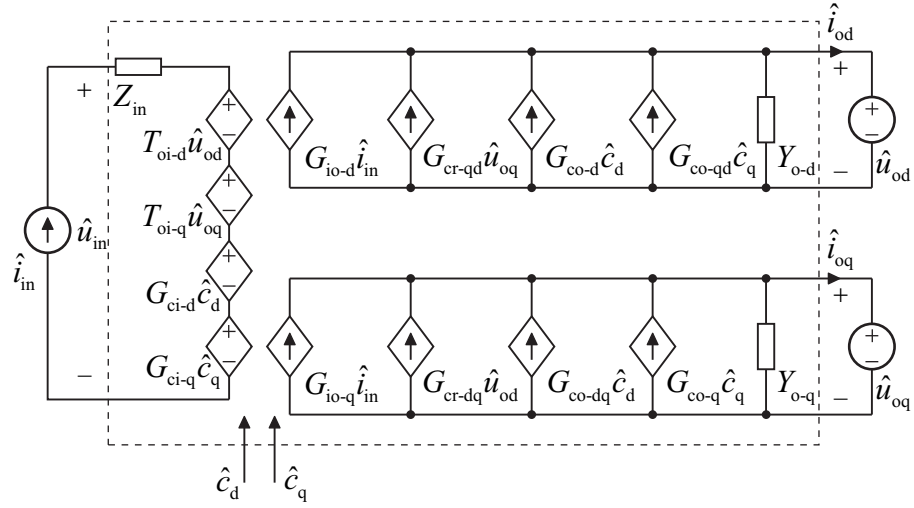


Figure 4.6: A linear network model for a two-level three-phase inverter.

A small-signal model of a two-level three-phase inverter under symmetrical and balanced grid conditions produces fifteen different transfer functions. In addition the resulting two output channels are coupled by their duty ratios and output voltages. Control block diagram of a cascaded control system implemented in a photovoltaic interfacing inverter is shown in Fig. 4.7. The decoupling has been omitted, but in case they were included, the diagram would be even more complicated.

It is evident from the figure that solving the closed-loop transfer function is demanding at the very least. However, a control block diagram can be used to find transfer functions, in which the controllers can be tuned.

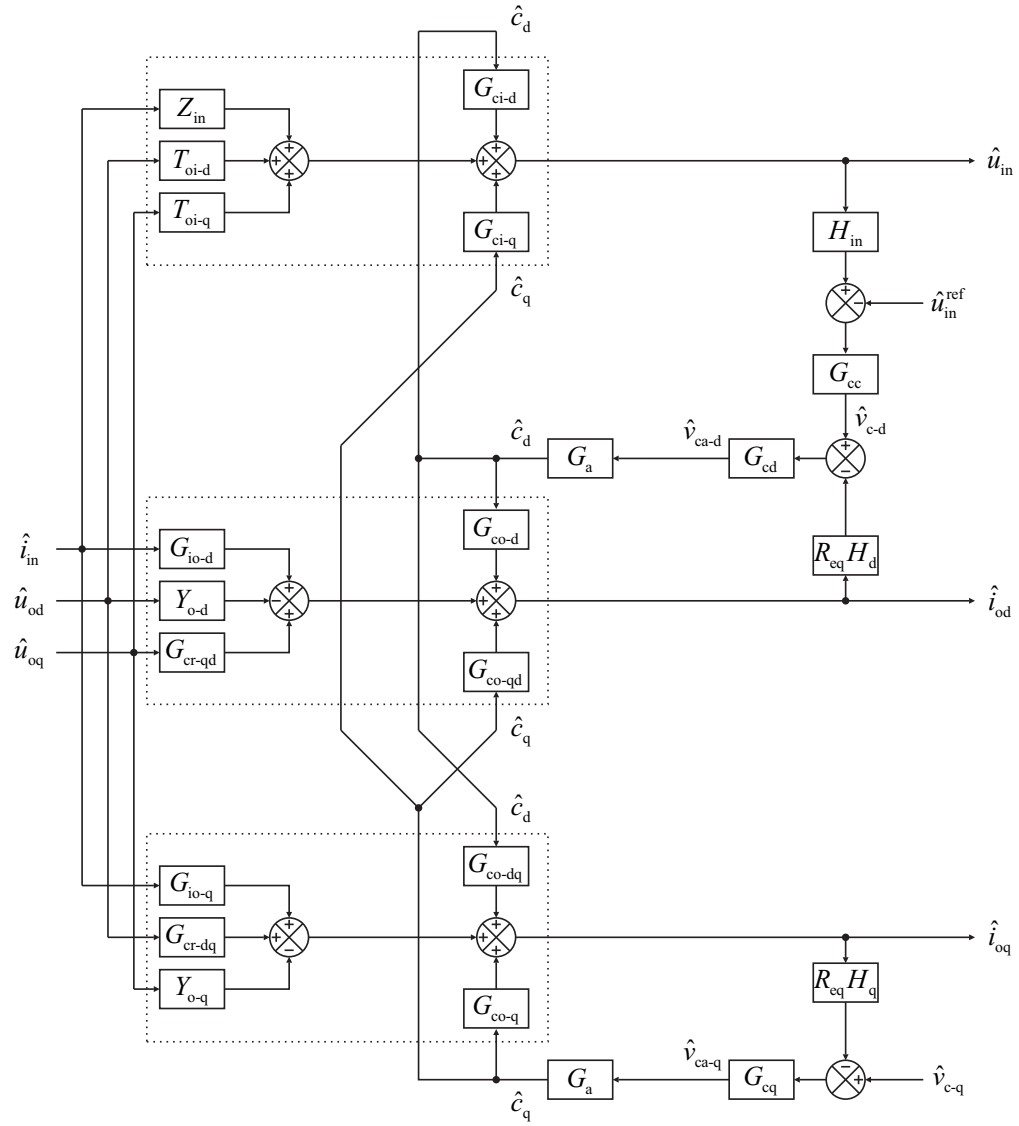


Figure 4.7: Control block diagram of a three-phase two-level inverter dq-model.

5. DYNAMICS OF A DC-EQUIVALENT CONVERTER

The small-signal representation of the two-level three-phase inverter in the synchronous reference frame connected to a symmetrical and balanced grid, produces fifteen different transfer functions. As stated above, the closed-loop transfer functions can not be easily solved due to cross-coupling between the d and q-channels. One way of reducing the complexity is to approximate the three-phase inverter with a reduced-order model. In [28] and [29], the three-phase inverter is transformed into a dc-equivalent circuit by replacing the inverter switches with modified transformers. It is also stated in [28] that the reduced order model can be constructed by ignoring the q-channel dynamics, because the d-channel accounts for the real power transfer, thus dominating the system dynamics.

A grid-tied PV interfacing inverter is usually operated at unity power factor, since its primary purpose is to feed real power to the utility grid. It is reasonable to assume that the current q-component is zero. In the previous analysis, balanced and symmetrical grid voltages were also assumed. When the q-channel dynamics are omitted and the cross-coupling effects between d and q-channels are weak, the three-phase inverter network model is simplified to contain only six transfer functions as depicted in Fig. 5.1. By inspection, this is exactly the same two-port model that was presented in Chapter 3 for the current-fed converter.

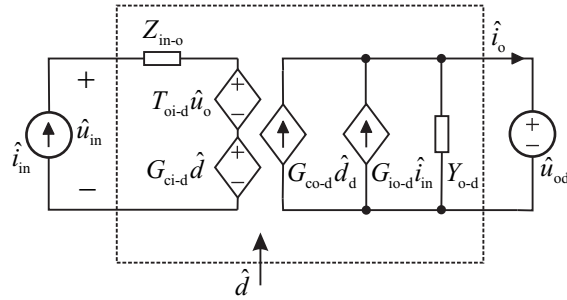


Figure 5.1: The simplified two-port model when dynamics associated to the q-channel are omitted.

The power stage of the resulting converter is shown in Fig. 5.2 with parasitics. In the following, this topology will be called as a dc-equivalent converter. The upper switch of the converter sw_1 conducts during the on-time, which means that its conduction time is proportional to the duty ratio d , and the lower switch is conducting during

off-time, thus its conduction time is proportional to the complement of the duty ratio d' . Current sensing resistors R_{s1} and R_{s2} are also included in the diagram, because they were included in the prototype converter which will be studied later.

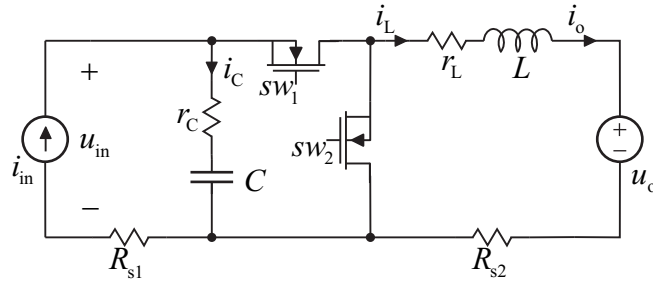


Figure 5.2: Power stage of the dc-equivalent converter.

5.1 Open-loop transfer functions

The procedure to obtain the transfer functions for the dc-equivalent converter is exactly the same as discussed in Chapter 3. The converter is assumed to operate in CCM. r_{ds1} and r_{ds2} are the parasitic resistances of switches sw_1 and sw_2 . Resulting two subcircuits with parasitic elements and current sensing resistors are shown in Fig. 5.3.

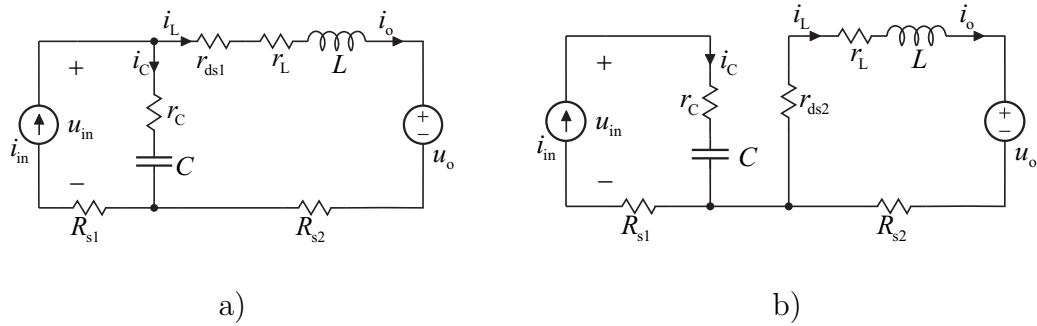


Figure 5.3: a) On-time and b) off-time subcircuit of the dc-equivalent converter.

Time derivative of the input capacitor voltage can be extracted by KCL and the time derivative of the inductor current by KVL. The input variables are the input current and the output voltage and the output variables are the input voltage and the output current. State variables are selected as the inductor current and the capacitor voltage. Time derivatives of the state variables and the output variables for on- and off-time subcircuits are presented in (5.1) and (5.2) as functions of the state and the input variables.

On-time equations:

$$\begin{aligned}
\frac{di_{L,\text{on}}}{dt} &= -\frac{(r_C + r_{\text{ds1}} + r_L + R_{\text{s2}})}{L}i_L + \frac{1}{L}u_C + \frac{r_C}{L}i_{\text{in}} - \frac{1}{L}u_o \\
\frac{du_{C,\text{on}}}{dt} &= -\frac{1}{C}i_L + \frac{1}{C}i_{\text{in}} \\
u_{\text{in,on}} &= -r_C i_L + u_C + (r_C + R_{\text{s1}}) i_{\text{in}} \\
i_{\text{o,on}} &= i_L
\end{aligned} \tag{5.1}$$

Off-time equations:

$$\begin{aligned}
\frac{di_{L,\text{off}}}{dt} &= -\frac{(r_L + r_{\text{ds2}} + R_{\text{s2}})}{L}i_L - \frac{1}{L}u_o \\
\frac{du_{C,\text{off}}}{dt} &= \frac{1}{C}i_{\text{in}} \\
u_{\text{in,off}} &= u_C + (r_C + R_{\text{s1}}) i_{\text{in}} \\
i_{\text{o,off}} &= i_L
\end{aligned} \tag{5.2}$$

Converter behavior can be averaged over one switching period by multiplying the on-time equations by the duty ratio d and the off-time equations by the complement of the duty ratio d' and summing the resulting equations together. This yields an averaged model as presented in (5.3).

$$\begin{aligned}
\frac{d\langle i_L \rangle}{dt} &= -\frac{(d(r_C + r_{\text{ds1}}) + r_L + d'r_{\text{ds2}} + R_{\text{s2}})}{L}\langle i_L \rangle + \frac{d}{L}\langle u_C \rangle + \frac{dr_C}{L}\langle i_{\text{in}} \rangle - \frac{1}{L}\langle u_o \rangle \\
\frac{d\langle u_C \rangle}{dt} &= -\frac{d}{C}\langle i_L \rangle + \frac{1}{C}\langle i_{\text{in}} \rangle \\
\langle u_{\text{in}} \rangle &= -dr_C \langle i_L \rangle + \langle u_C \rangle + (r_C + R_{\text{s1}}) \langle i_{\text{in}} \rangle \\
\langle i_o \rangle &= \langle i_L \rangle
\end{aligned} \tag{5.3}$$

The steady-state operating point can be solved from (5.3) by setting derivative terms to zero. These are shown in (5.4) and (5.5) for the capacitor voltage and the inductor current. Second order polynomial is obtained for the duty cycle steady-state value, which can be solved as in (5.6).

$$I_L = \frac{I_{\text{in}}}{D} \tag{5.4}$$

$$U_C = U_{\text{in}} - R_{\text{s1}} I_{\text{in}} \tag{5.5}$$

$$D = \frac{-b + \sqrt{b^2 - 4ac}}{2a}, \tag{5.6}$$

where the coefficients for the second order polynomial are

$$\begin{aligned}
a &= U_{\text{in}} + I_{\text{in}}(r_C - R_{\text{s1}}) \\
b &= (r_{\text{ds2}} - r_C - r_{\text{ds1}}) I_{\text{in}} - U_o \\
c &= -(r_L + r_{\text{ds2}} + R_{\text{s2}}) I_{\text{in}}
\end{aligned}$$

Linearized small-signal model can be produced from (5.3) by introducing first order partial derivatives with respect to all variables. This yields a linearized small-signal model as presented in (5.7) where the hat over a variable denotes a small ac-perturbation around the operating point.

$$\begin{aligned}
\frac{d\hat{i}_L}{dt} &= -\frac{R_{eq}}{L}\hat{i}_L + \frac{D}{L}\hat{u}_C + \frac{Dr_C}{L}\hat{i}_{in} - \frac{1}{L}\hat{u}_o + \frac{U_{eq}}{L}\hat{d} \\
\frac{d\hat{u}_C}{dt} &= -\frac{D}{C}\hat{i}_L + \frac{1}{C}\hat{i}_{in} - \frac{I_{in}}{DC}\hat{d} \\
\hat{u}_{in} &= -Dr_C\hat{i}_L + \hat{u}_C + (r_C + R_{s1})\hat{i}_{in} - \frac{r_C I_{in}}{D}\hat{d} \\
\hat{i}_o &= \hat{i}_L
\end{aligned} \tag{5.7}$$

where

$$\begin{aligned}
R_{eq} &= D(r_C + r_{ds1}) + r_L + R_{s2} + D'r_{ds2} \\
U_{eq} &= \frac{-(r_C + r_{ds1} - r_{ds2})I_{in}}{D} + U_{in} + I_{in}(r_C - R_{s1})
\end{aligned}$$

The linearized small-signal model of (5.7) can be presented in a matrix form as in (5.8) and the dynamic profile of the converter solved by using (2.10). This yields a set of transfer functions describing the small-signal relations between the input- and output variables of the converter as presented in (5.9). Transfer functions from input to output variables of the dc-equivalent converter, when parasitics and current sensing resistors are neglected, are presented in (5.10) - (5.15). Δ is the characteristic polynomial of the converter.

$$\begin{aligned}
\begin{bmatrix} \frac{d\hat{i}_L}{dt} \\ \frac{d\hat{u}_C}{dt} \end{bmatrix} &= \begin{bmatrix} -\frac{R_{eq}}{L} & \frac{D}{L} \\ -\frac{D}{C} & 0 \end{bmatrix} \begin{bmatrix} \hat{i}_L \\ \hat{u}_C \end{bmatrix} + \begin{bmatrix} \frac{Dr_C}{L} & -\frac{1}{L} & \frac{U_{eq}}{L} \\ \frac{1}{C} & 0 & -\frac{I_{in}}{DC} \end{bmatrix} \begin{bmatrix} \hat{i}_{in} \\ \hat{u}_o \\ \hat{d} \end{bmatrix} \\
\begin{bmatrix} \hat{u}_{in} \\ \hat{i}_o \end{bmatrix} &= \begin{bmatrix} -Dr_C & 1 \\ 1 & 0 \end{bmatrix} \begin{bmatrix} \hat{i}_L \\ \hat{u}_C \end{bmatrix} + \begin{bmatrix} (r_C + R_{s1}) & 0 & -\frac{r_C I_{in}}{D} \\ 0 & 0 & 0 \end{bmatrix} \begin{bmatrix} \hat{i}_{in} \\ \hat{u}_o \\ \hat{d} \end{bmatrix}
\end{aligned} \tag{5.8}$$

$$\begin{bmatrix} \hat{u}_{in} \\ \hat{i}_o \end{bmatrix} = \begin{bmatrix} Z_{in-o} & T_{oi-o} & G_{ci-o} \\ G_{io-o} & -Y_{o-o} & G_{co-o} \end{bmatrix} \begin{bmatrix} \hat{i}_{in} \\ \hat{u}_o \\ \hat{d} \end{bmatrix} \tag{5.9}$$

$$\Delta Z_{\text{in-o}} = \frac{s}{C} \quad (5.10)$$

$$\Delta T_{\text{oi-o}} = \frac{D}{LC} \quad (5.11)$$

$$\Delta G_{\text{ci-o}} = -\frac{I_{\text{in}}}{DC} \left(s + \frac{D^2 U_{\text{in}}}{L I_{\text{in}}} \right) \quad (5.12)$$

$$\Delta G_{\text{io-o}} = \frac{D}{LC} \quad (5.13)$$

$$\Delta Y_{\text{o-o}} = \frac{s}{L} \quad (5.14)$$

$$\Delta G_{\text{co-o}} = \frac{U_{\text{in}}}{L} \left(s - \frac{I_{\text{in}}}{C U_{\text{in}}} \right) \quad (5.15)$$

$$\Delta = s^2 + \frac{D^2}{LC} \quad (5.16)$$

Transfer functions of the dc-equivalent converter can be compared with those representing the d-channel and input dynamics of the three-phase two-level inverter shown in (4.31)-(4.45). The coefficients of these two models are quite similar, with a scaling factor $3/2$ appearing in the inverter dq-model transfer functions introduced by the use of the space-vector transformation. In addition, the grid angular frequency ω_s and the duty ratio q-component are not present in transfer functions of the dc-equivalent converter. The order of the transfer functions is reduced to two. It is noticeable that the RHP-zero is exactly at the same angular frequency $I_{\text{in}}/C U_{\text{in}}$ in both of the models.

As mentioned previously in Chapter 2, two different space-vector transformations exists, namely power- and amplitude invariant versions. The transformation used in this thesis is the amplitude invariant version. Before the two models can be compared, their power levels need to be scaled to be equal. In other words, the output voltage of the dc-equivalent circuit needs to be scaled.

According to [30], the real power in an amplitude invariant space-vector transformed three-phase system is

$$p = \frac{3}{2} \text{Re} \{ \underline{u} \underline{i}^* \}, \quad (5.17)$$

where \underline{i}^* denotes a complex conjugate of the current vector.

The average output power in the synchronous reference frame can be presented as in (5.18). Noticing that the current and voltage q-components are zero and setting the output powers of the inverter model in the synchronous reference frame and the dc-equivalent converter equal, yields a new presentation for the output voltage of the dc-equivalent converter as shown in (5.19):

$$P_o = \frac{3}{2} \operatorname{Re} \{ \underline{U}_o \underline{I}_o^* \} = \frac{3}{2} (U_{od} I_{od} + U_{oq} I_{oq}) = \frac{3}{2} U_{od} I_{od} \quad (5.18)$$

$$\begin{aligned} \Rightarrow \quad & \frac{3}{2} U_{od} I_{od} = I_o U_o \\ & \frac{3}{2} U_{od} \frac{2I_{in}}{3D_d} = \frac{I_{in}}{D} U_o \\ \Rightarrow \quad & U_o = \frac{D}{D_d} U_{od} \end{aligned} \quad (5.19)$$

The duty ratio can be solved by inserting (5.19) to the averaged model of the dc-equivalent converter (5.3). The value of the duty ratio in the dc-equivalent model depends now on the output voltage of the d-channel U_{od} and the direct component of the duty ratio D_d rather than on the original output voltage U_o . The obtained representation for the dc-model duty ratio is as shown in (5.20). The subscript 'd' denotes, that the coefficients depend on the d-channel steady state values.

$$D = \frac{-b_d + \sqrt{b_d^2 - 4a_d c_d}}{2a_d}, \quad (5.20)$$

where the coefficients are

$$\begin{aligned} a_d &= U_{in} - \frac{U_{od}}{D_d} + (r_C - R_{s1}) I_{in} \\ b_d &= -(r_C + r_{ds1} - r_{ds2}) I_{in} \\ c_d &= -(r_L + r_{ds2} + R_{s2}) I_{in} \end{aligned}$$

The proper output voltage for the dc-equivalent coverter can be solved by inserting the duty ratio of (5.20) to (5.19), which gives the relation between the two models.

Transfer functions resulting from the inverter model in the synchronous reference frame and the dc-equivalent converter were plotted and compared using MATLAB software package. Parasitic resistances were included in both of the models and the voltage of the dc-equivalent converter was scaled, according to (5.19), to match the power levels in both systems. Input current sensing resistor was neglected, because it was not included in the inverter model. Figs. 5.4 and 5.5 show how the input impedances and d-channel output admittances of the three-phase inverter and the dc-equivalent converter correlate¹.

According to the results so far, the dc-equivalent converter can be used with good accuracy to model the inverter d-channel- and input dynamics of the three-phase inverter.

¹For reducing the pages, the rest of the results are collected in Appendix A.

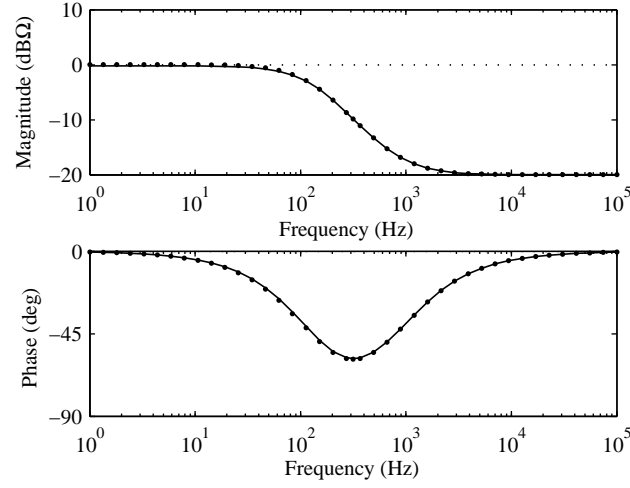


Figure 5.4: Estimated input impedances from inverter dq-model (dotted line) and the dc-equivalent model (solid line).

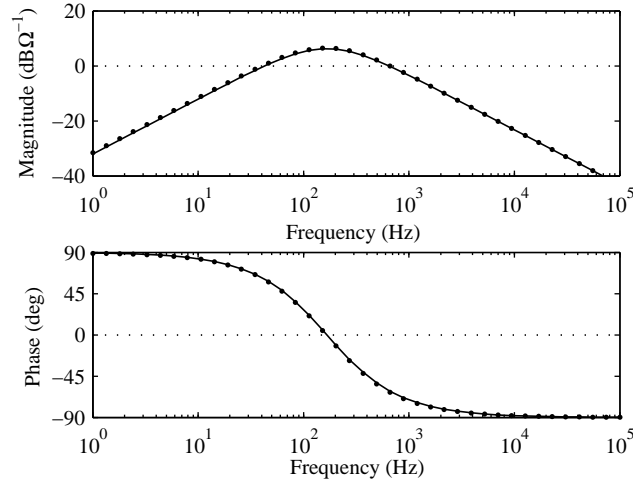


Figure 5.5: Estimated output admittances from inverter d-channel (dotted line) and the dc-equivalent model (solid line).

5.2 Closed-loop transfer functions

Input and output dynamics of the dc-equivalent model can be extracted from (5.9) and written as in (5.21) and (5.22). From these a control block diagram can be constructed when a cascaded control system is used, as shown in Figs. 5.6 and 5.7.

$$\hat{u}_{in} = Z_{in-o}\hat{i}_{in} + T_{oi-o}\hat{u}_o + G_{ci-o}\hat{d} \quad (5.21)$$

$$\hat{i}_o = G_{io-o}\hat{i}_{in} - Y_{o-o}\hat{u}_o + G_{co-o}\hat{d} \quad (5.22)$$

Since the converter is used to model the dynamics of the three-phase inverter, a cascaded control structure is implemented as discussed in Chapter 4. The outer loop controls the input voltage and produces a reference value for the inner output current

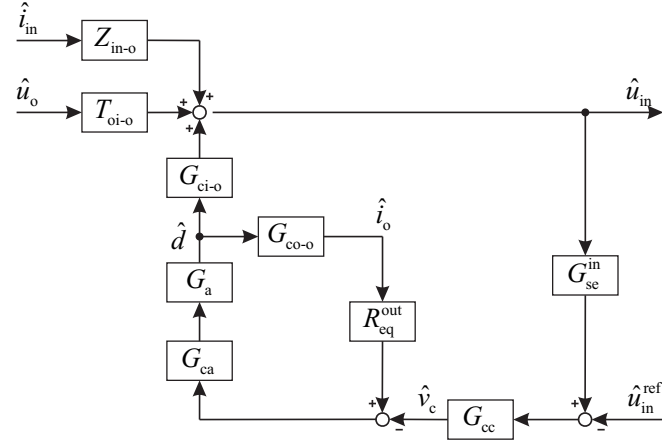


Figure 5.6: Input dynamics control block diagram of a dc-equivalent converter with a cascaded control system.

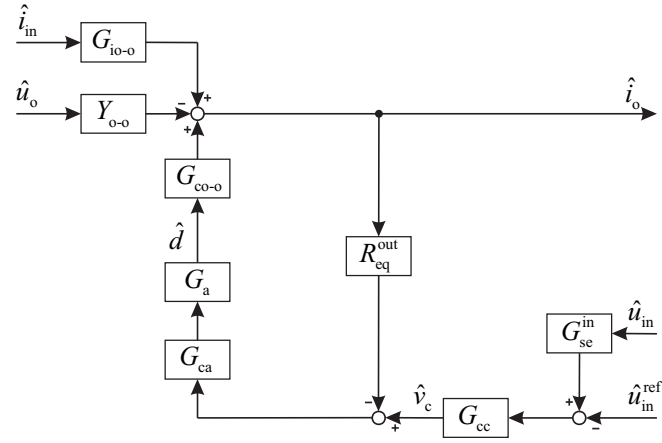


Figure 5.7: Output dynamics control block diagram of a dc-equivalent converter with a cascaded control system.

control loop. The voltage controller of the outer loop is denoted by G_{cc} and the current controller of the inner loop by G_{ca} . Sensing gains related to input voltage and output current are denoted by G_{se}^{in} and R_{eq}^{out} respectively. G_a is the gain related to the pulse width modulator (PWM). \hat{v}_c is the control voltage from the input voltage controller, which is fed as a reference voltage to the current controller.

The closed-loop transfer functions can be solved from the input and output dynamics control block diagrams. Most convenient way of doing this is to consider at first the system without the input voltage control. Thus, only the inner output current control loop is connected as shown in Fig. 5.8. Now the closed-loop transfer functions with output current control can be solved as shown in (5.23) - (5.28). The superscript 'out' is used to denote that only the output current control is connected.

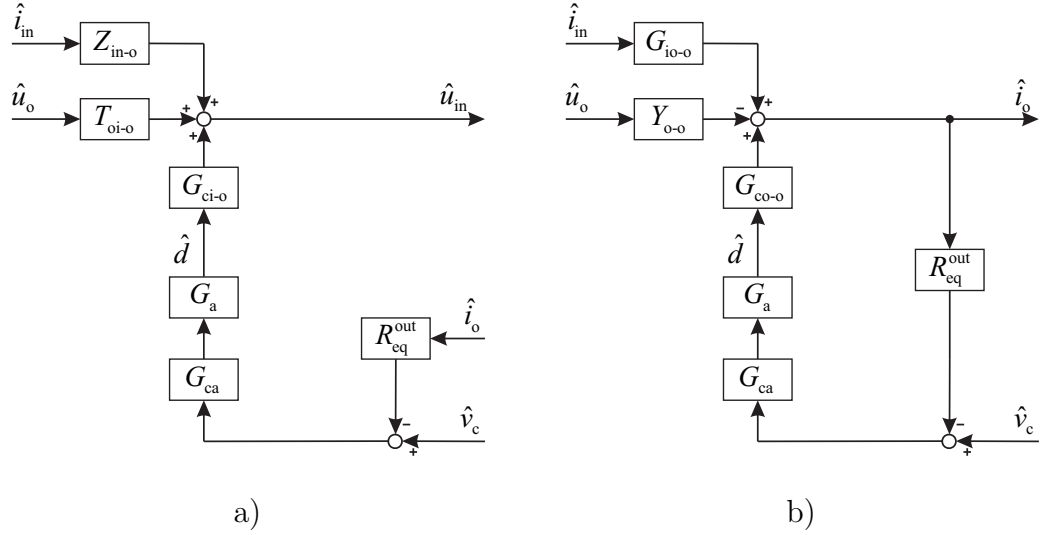


Figure 5.8: a) Input and b) output dynamics control block diagrams of the converter when the input voltage control is disconnected.

Closed-loop transfer functions with output current control:

$$Z_{in-c}^{out} = \frac{Z_{in-o}}{1 + L_{out}} + \frac{L_{out}}{1 + L_{out}} Z_{in-\infty} \quad (5.23)$$

$$T_{oi-c}^{out} = \frac{T_{oi-o}}{1 + L_{out}} + \frac{L_{out}}{1 + L_{out}} T_{oi-\infty} \quad (5.24)$$

$$G_{ri}^{out} = \frac{1}{R_{eq}^{out}} \frac{L_{out}}{1 + L_{out}} \frac{G_{ci-o}}{G_{co-o}} \quad (5.25)$$

$$G_{io-c}^{out} = \frac{G_{io-o}}{1 + L_{out}} \quad (5.26)$$

$$Y_{o-c}^{out} = \frac{Y_{o-o}}{1 + L_{out}} \quad (5.27)$$

$$G_{ro}^{out} = \frac{1}{R_{eq}^{out}} \frac{L_{out}}{1 + L_{out}}, \quad (5.28)$$

where

$$\begin{aligned} Z_{in-\infty} &= Z_{in-o} - \frac{G_{ci-o} G_{io-o}}{G_{co-o}} \\ T_{oi-\infty} &= T_{oi-o} + \frac{G_{ci-o} Y_{o-o}}{G_{co-o}} \\ L_{out} &= R_{eq}^{out} G_{ca} G_{co-o} G_a \end{aligned}$$

are the ideal input impedance, ideal output-to-input transmittance and the current control loop gain.

The input voltage control is included by considering the output current controlled converter as an open-loop system for the voltage control. Resulting control block diagrams for input- and output dynamics are as depicted in Fig. 5.9. The closed-loop transfer functions, with both control loops connected, are presented in (5.29) - (5.34).

Superscript 'out-in' is used to denote that both loops, the output current and the input voltage, are connected.

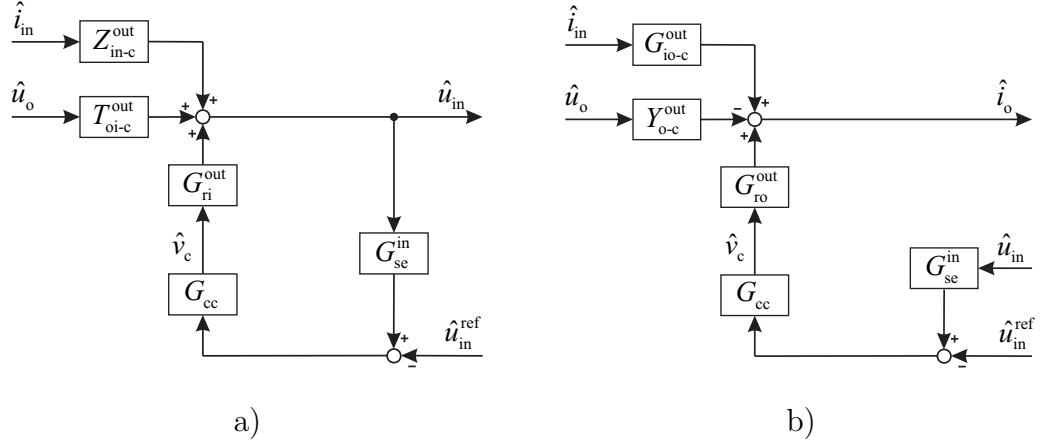


Figure 5.9: a) Input and b) output dynamics control block diagrams of the converter when the input voltage control loop is inserted to output current controlled converter.

Closed-loop transfer functions for the converter when both control loops are connected:

$$Z_{in-c}^{out-in} = \frac{Z_{in-o}}{(1 + L_{out})(1 - L_{in})} + \frac{L_{out}}{(1 + L_{out})(1 - L_{in})} Z_{in-\infty} \quad (5.29)$$

$$T_{oi-c}^{out-in} = \frac{T_{oi-o}}{(1 + L_{out})(1 - L_{in})} + \frac{L_{out}}{(1 + L_{out})(1 - L_{in})} T_{oi-\infty} \quad (5.30)$$

$$G_{ri}^{out-in} = -\frac{1}{G_{se}^{in}} \frac{L_{in}}{1 + L_{in}} \quad (5.31)$$

$$G_{io-c}^{out-in} = \frac{G_{io-o}}{(1 + L_{out})(1 - L_{in})} - \frac{L_{in}}{1 - L_{in}} G_{io-\infty} \quad (5.32)$$

$$Y_{o-c}^{out-in} = \frac{Y_{o-o}}{(1 + L_{out})(1 - L_{in})} - \frac{L_{in}}{1 - L_{in}} Y_{o-\infty} \quad (5.33)$$

$$G_{ro}^{out-in} = -\frac{1}{G_{se}^{in}} \frac{L_{in}}{1 + L_{in}} \frac{G_{co-o}}{G_{ci-o}}, \quad (5.34)$$

where

$$\begin{aligned}
Z_{in-\infty} &= Z_{in-o} - \frac{G_{ci-o}G_{io-o}}{G_{co-o}} \\
T_{oi-\infty} &= T_{oi-o} + \frac{G_{ci-o}Y_{o-o}}{G_{co-o}} \\
G_{io-\infty} &= G_{io-o} - \frac{G_{co-o}Z_{in-o}}{G_{ci-o}} \\
Y_{o-\infty} &= Y_{o-o} + \frac{G_{co-o}T_{oi-o}}{G_{ci-o}} \\
L_{out} &= R_{eq}^{out} G_{ca} G_{co-o} G_a \\
L_{in} &= \frac{G_{se}^{in}}{R_{eq}^{out}} \frac{L_{out}}{1 + L_{out}} \frac{G_{ci-o}}{G_{co-o}} G_{cc}
\end{aligned}$$

are the ideal input impedance, ideal output-to-input transmittance, ideal input-to-output transfer function, ideal output admittance, output current control loop and input voltage control loop.

It has to be noted that the output current control loop includes RHP-zero due to G_{co-o} , which turns into RHP-pole in the input voltage loop when the outer loop is connected. The input voltage control loop can be simplified to (5.35), where the loop now has a RHP-pole due to G_{co-o} . This adds limitations to control design, which will be discussed later.

$$L_{in} = \frac{G_{se}^{in} G_{ca} G_a G_{ci-o} G_{cc}}{1 + R_{eq}^{out} G_{ca} G_{co-o} G_a} \quad (5.35)$$

6. EFFECT OF PHOTOVOLTAIC GENERATOR ON CONVERTER DYNAMICS

6.1 Electrical properties of a photovoltaic cell

By physical structure a photovoltaic cell is a pn-junction similar to a diode. A current is generated at the junction when the cell is exposed to sunlight. The most commonly used equivalent circuit for a photovoltaic cell is the one-diode version [31] as depicted in Fig. 6.1.

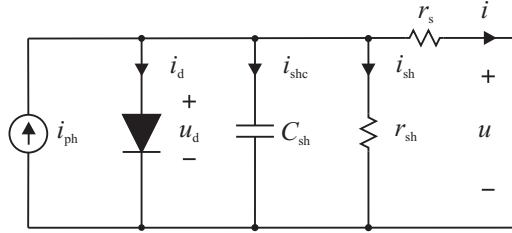


Figure 6.1: One-diode equivalent circuit of a photovoltaic cell.

Current source i_{ph} models the photocurrent created by sunlight, diode models the properties of the actual pn-junction, r_s is a structural resistance of the PV cell, r_{sh} models leakage current through the pn-junction and capacitor C_{sh} models a parasitic capacitance of the pn-junction. The value of the parasitic capacitance is small and is usually neglected to simplify analysis. The resulting current-voltage characteristics of the PV cell, neglecting the parasitic capacitance, can be presented as shown in (6.1) [13].

$$i = i_{ph} - i_o \left[\exp \left(\frac{u + r_s i}{A k T / q} \right) - 1 \right] - \frac{u + r_s i}{r_{sh}}, \quad (6.1)$$

where A is diode ideality factor, k Boltzmann constant, q elementary charge and T temperature of the pn-junction.

It is obvious that the PV generator, constituting of several cells connected in series and parallel, is a highly non-linear and non-ideal source [32]. Thus it can not be modeled with an ideal voltage or current source. A typical current-voltage curve of a PV cell with output power and operation point dependent dynamic resistance is depicted in Fig. 6.2.

From Fig. 6.2 it can be seen that the PV cell resembles a current source at the

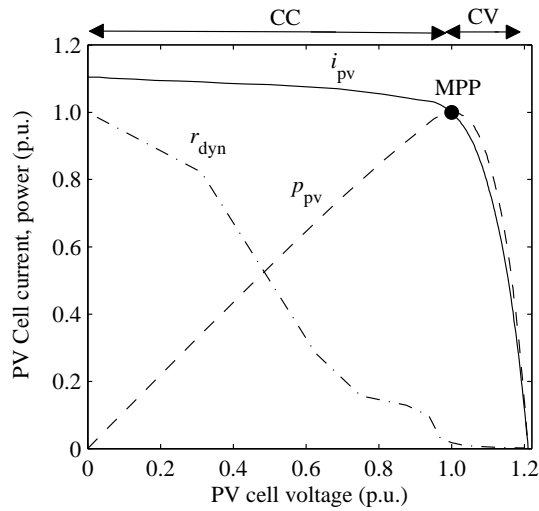


Figure 6.2: Terminal characteristics of a typical photovoltaic cell.

voltages below the MPP voltage and a voltage source at the voltages above the MPP voltage. In this thesis, these regions will be called constant current (CC) region and constant voltage (CV) region. Between these two regions is a point where the output power reaches its maximum value. This point is called a maximum power point (MPP) accordingly.

A PV generator is typically formed by connecting multiple cells in series and parallel to meet the required output voltage and current levels. The PV generator can be modeled as a parallel combination of a photocurrent source and a dynamic resistance r_{dyn} as depicted in Fig. 6.3. The value of the dynamic resistance depends on the operating point. At low voltages the dynamic resistance is high and the PV generator resembles a current source. At higher voltages, the dynamic resistance becomes smaller and the PV generator voltage reaches its maximum at open circuit. Thus the PV generator resembles a voltage source.

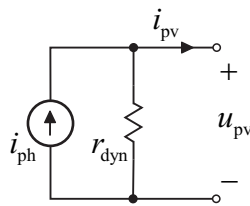


Figure 6.3: A simplified equivalent circuit of a photovoltaic generator.

6.2 Effect of photovoltaic generator on open-loop dynamics

The effect of a PV generator on the dynamics of the dc-equivalent converter can be approximated by using the simplified circuit of Fig. 6.3 for the PV generator. Source affected transfer functions can be solved according to (2.13), noticing that $Y_S = 1/r_{dyn}$.

Measured output impedance of a Raloss SR30-36 solar module in different operation points along the I - U -curve, when exposed to a light source with irradiation of $500\text{W}/\text{m}^2$ [32], is depicted in Fig. 6.4. The output impedance resembles a pure resistor at low frequency which supports the use of the simplified circuit for the PV generator in Fig. 6.3.

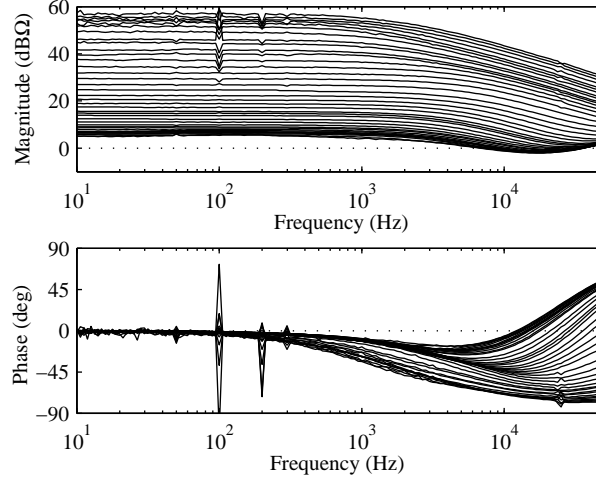


Figure 6.4: Measured output impedance of Raloss SR30-36 solar module.

To validate the results, a prototype converter according to Fig. 5.2 was constructed. The prototype included also low-pass filtered measurement circuits for input and output voltages and currents. Switching frequency was selected to be 100 kHz and corner frequency for the measurement circuits 50 kHz. Control system was implemented using Texas Instruments digital signal processor eZdsp F28335. Frequency responses were extracted using Venable Industries' frequency response analyzer Model 3120. Component values for the prototype are listed in Table 6.1. More information about the prototype converter and the test setup can be found from Appendix C.

Source affected control-to-output transfer function can be calculated as in (6.2) where superscript 'S' denotes that the transfer function is affected by the non-ideal source.

$$G_{\text{co-o}}^{\text{S}} = \frac{1 + Y_{\text{S}} Z_{\text{in-}\infty}}{1 + Y_{\text{S}} Z_{\text{in-o}}} G_{\text{co-o}}, \quad (6.2)$$

where

$$Y_{\text{S}} = \frac{1}{r_{\text{dyn}}}$$

$$Z_{\text{in-}\infty} = Z_{\text{in-o}} - \frac{G_{\text{io-o}} G_{\text{ci-o}}}{G_{\text{co-o}}}$$

are the source admittance and the ideal input impedance.

Measured and predicted control-to-output transfer functions at open loop in the CC and CV regions of the PV generator are shown in Fig. 6.5. Increasing phase-lag

Table 6.1: Component values for the prototype converter.

Component	Value
C	2.2 mF
L	220 μ H
R_{s1}	0.1 Ω
R_{s2}	0.1 Ω

at high frequencies is due to the delay introduced by the DSP and was included to the model as a first order Pade approximation (6.3).

$$G_{\text{delay}} = \frac{1 - \frac{T_s}{2}s}{1 + \frac{T_s}{2}s} \quad (6.3)$$

The phase of the transfer function starts from 180 degrees in the CC region and from zero degrees in the CV region. Such a behavior can be understood by considering the source-affected control-to-output current transfer function without parasitics. Equation (6.2) can be written without parasitics as shown in (6.4).

$$G_{\text{co-o}}^S = \frac{U_{\text{in}} \left[s + \frac{1}{C} \left(\frac{1}{r_{\text{dyn}}} - \frac{I_{\text{in}}}{U_{\text{in}}} \right) \right]}{L \left(s^2 + \frac{1}{Cr_{\text{dyn}}}s + \frac{D^2}{LC} \right)} \quad (6.4)$$

It can be seen directly that when the static admittance of the converter $I_{\text{in}}/U_{\text{in}}$ is greater than the source admittance $1/r_{\text{dyn}}$ the zero of the control-to-output transfer function becomes positive. This happens when operating point crosses the MPP to the CC region, because at the MPP the dynamic resistance of the PV generator equals the static resistance of the converter according to the maximum power transfer theorem. In other words, the RHP-zero appears when the operation point is moved over the MPP to the CC region. Due to this phase flip, a single loop output current control which is stable in all operation points can not be implemented. For example, a high bandwidth current control designed in the CV region would become unstable in the CC region because the bandwidth should be limited below the frequency of the RHP-zero [33]. In addition, because the RHP-zero is at low frequencies, a control system with just a few hertz of bandwidth would be of no practical value. In addition, the control signal should be inverted in the CC and noninverted in the CV region.

The source affected control-to-input-voltage transfer function is as shown in (6.5).

$$G_{\text{ci-o}}^S = \frac{G_{\text{ci-o}}}{1 + Y_S Z_{\text{in-o}}} \quad (6.5)$$

The parasitic resistance of the PV generator has negligible effect on the transfer function. Control-to-input voltage transfer function is depicted in Fig. 6.6.

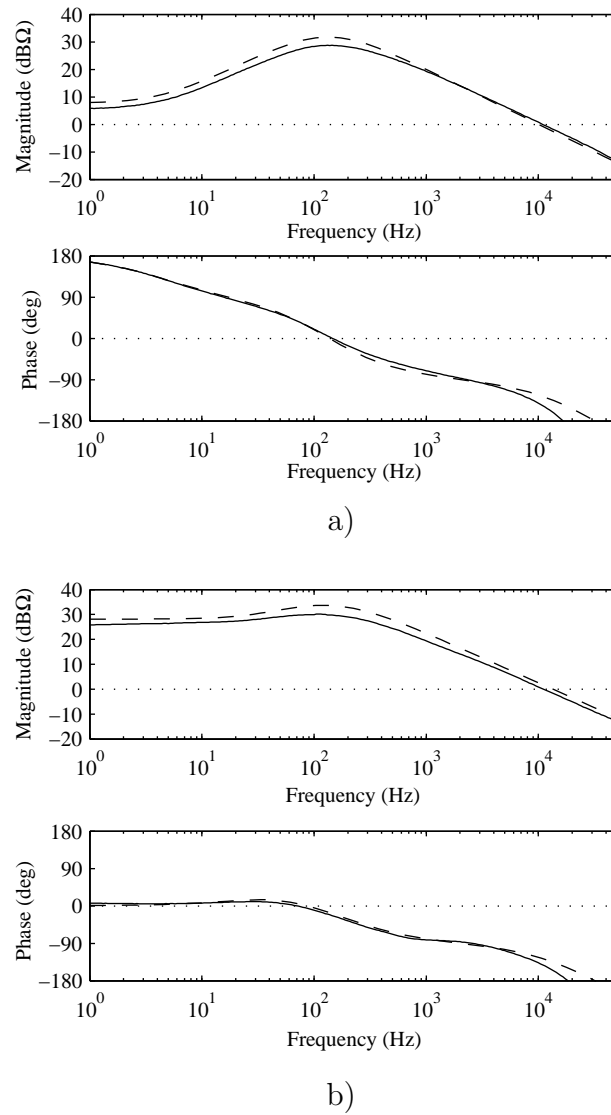


Figure 6.5: Measured (solid) and predicted (dashed) control-to-output current transfer functions in a) constant current region and b) constant voltage regions.

The phase in Fig. 6.6 starts from 180, which implies that either the low side switch should be on-time controlled or the control signal in the voltage controller inverted. The latter option was chosen, because the dynamical analysis was done for the case where the high side switch is on-time controlled.

6.3 Control system design

The phase flip of G_{co-o}^S makes it impossible to operate the converter in all operating points of the I - U -curve when only output current control is active as discussed in the previous section. On the other hand, the input voltage has to be controlled to provide maximum power point tracking (MPPT). In addition, the output current needs to be controlled to comply with the grid codes if the inverter is connected to the utility grid. A cascaded control structure is usually implemented in grid-connected inverters and a control system of the same type was designed for the dc-equivalent converter [23]. The

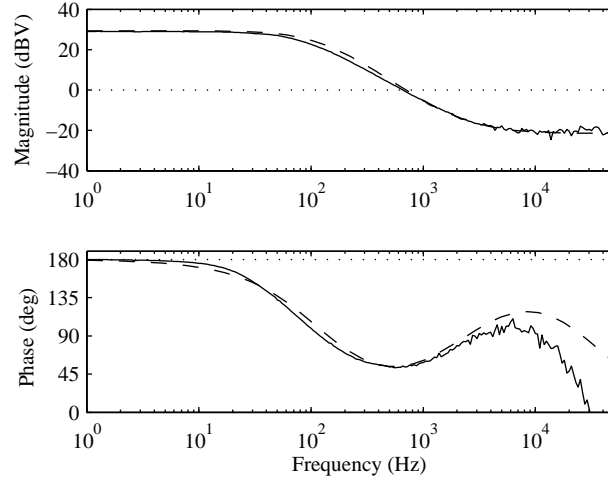


Figure 6.6: Measured (solid) and predicted (dashed) control-to-input voltage transfer function at open loop.

inner loop controls the output current and the outer loop the input voltage as depicted in Fig. 6.7.

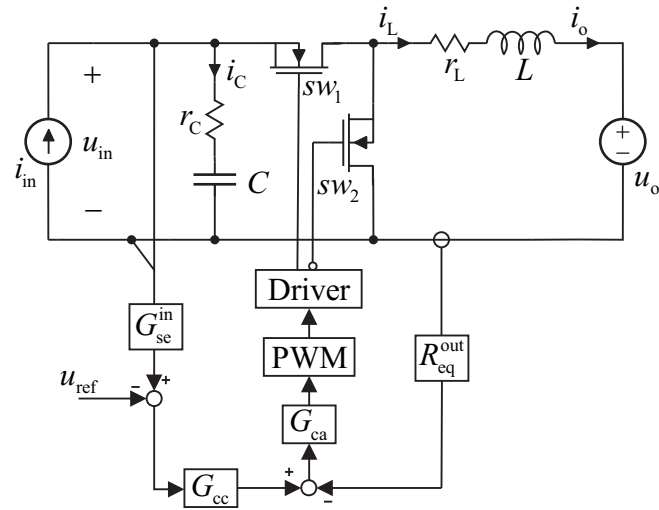


Figure 6.7: Cascaded control system implemented to the dc-dc converter.

The current control loop can be solved from control block diagram in Fig. 5.8b and is found to be as in (6.6). Superscript 's' in G_{co-o}^s denotes that it is affected by the dynamic resistance of the PV generator.

$$L_{out} = R_{eq}^{out} G_{co-o}^s G_{ca} G_a \quad (6.6)$$

The current sensing transfer function R_{eq}^{out} in (6.7) includes low-pass filtering, gain introduced by the AD conversion, computing delay introduced by the DSP, and a scaling factor. Scaling is necessary, because the maximum voltage at the DSP pin is

restricted to 3 V. The delay originating from AD conversion is approximated using the first-order Pade approximation (6.3). G_{ca} is the current controller transfer function as shown in (6.8). G_a is the effective gain of the PWM process (1/1500) which is a property of finite resolution of the PWM used inside the DSP. f_{LP} is the corner frequency of the low-pass filter and is set to half the switching frequency (50 kHz).

$$R_{eq}^{out} = 0.8525 \cdot \frac{4096}{3} \cdot \frac{1}{1 + \frac{s}{2\pi f_{LP}}} G_{delay} \quad (6.7)$$

$$G_{ca} = K_{out} \frac{(s + \omega_{z-out})}{s(s/\omega_{p-out} + 1)} \quad (6.8)$$

Controller zero was placed at 1 kHz and pole at 25 kHz. The controller gain was set to 0.5 to achieve high enough control bandwidth of around 5 kHz. Resulting current control loop gain is shown in Fig. 6.8. The designed current control can not work in the CC region as such but the outer voltage control loop has to be connected as will be discussed later.

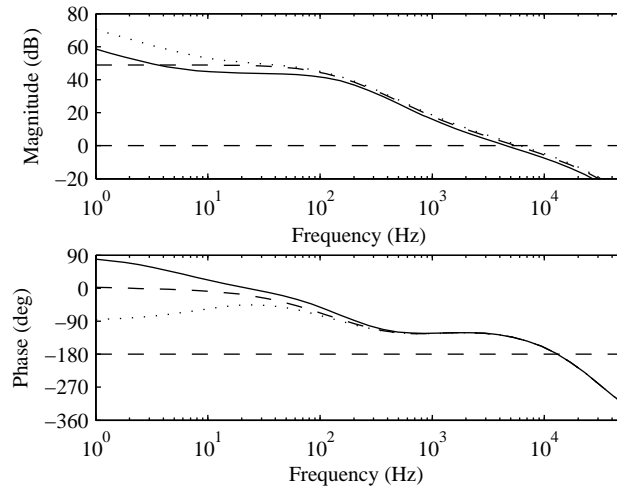


Figure 6.8: Predicted current control loop gain in CC region (solid), MPP (dashed) and CV region (dash-dotted) when input voltage control is disconnected.

Output-current-controlled converter is to be considered as an open-loop system when designing the input-voltage control. The third input variable is now the control voltage \hat{v}_c rather than the duty ratio \hat{d} according to Fig. 5.9. The transfer functions between control voltage and input voltage is as shown in (6.9).

$$G_{ri}^{out} = \frac{1}{R_{eq}^{out}} \frac{L_{out}}{1 + L_{out}} \frac{G_{ci-o}}{G_{co-o}} \quad (6.9)$$

The control-to-input-voltage transfer function (6.9) includes the current loop L_{out} and has the control-to-output-current transfer function in the denominator. As a consequence, the transfer function has a single RHP-pole in the CC region. According to

[33], the control bandwidth has to be higher than the frequency of the RHP-pole for the loop to be stable. The RHP-pole frequency is around 5 Hz. The voltage control bandwidth has to be higher than this, but low enough to provide attenuation at three times the grid frequency. The voltage control loop is as shown in (6.10).

$$L_{in} = \frac{1}{R_{eq}^{out}} \frac{L_{out}}{1 + L_{out}} \frac{G_{ci-o}}{G_{co-o}} G_{se}^{in} G_{cc}, \quad (6.10)$$

where G_{se}^{in} is the input-voltage-sensing transfer function (6.11) and G_{cc} the input-voltage-controller transfer function (6.12), which has the same form as the current controller.

$$G_{se}^{in} = 0.1102 \cdot \frac{4096}{3} \cdot \frac{1}{1 + \frac{s}{2\pi f_{LP}}} G_{delay} \quad (6.11)$$

$$G_{ca} = K_{in} \frac{(s + \omega_{z-in})}{s(s/\omega_{p-in} + 1)}, \quad (6.12)$$

The input voltage controller zero was placed at 10 Hz and pole at 50 Hz. The controller pole was placed at low frequency to attenuate 300Hz ripple which is always present in a grid-tied three-phase inverter. The gain of the controller was set to 3.98, which gives a control bandwidth of around 20 Hz. Control loop would attenuate the 300 Hz ripple by 40 dB. The resulting voltage control loop is given in Fig. 6.9 at different operating points.

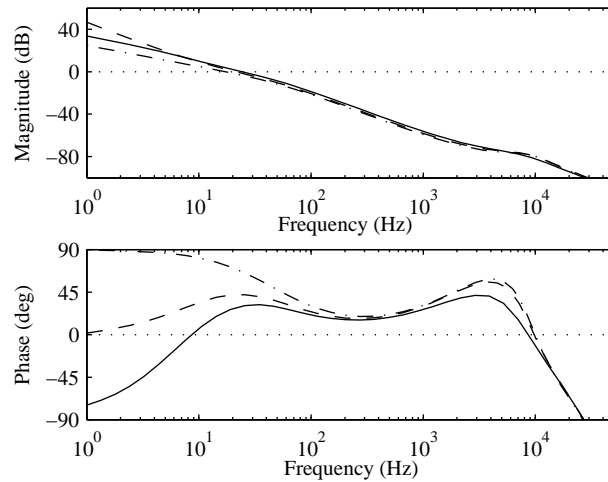


Figure 6.9: Predicted input voltage control loop gain in CC region (solid), MPP (dashed) and CV region (dash-dotted).

It has to be noted that the stability margins are analyzed in respect to 0 degrees line, since the reference is connected to the negative and the measurement to the positive part of the summer as was depicted in Fig. 6.9. The phase margin is lowest in the CC region and highest in the CV region. Thus the control system is expected to have

slowest settling times in the CC region. The achievable control bandwidth is limited by the need for attenuation at grid harmonics around 300 Hz for a three-phase inverter and cannot be increased much.

6.4 Effect of a photovoltaic generator on closed-loop dynamics

The closed loop output admittance of the dc-equivalent circuit was derived in Chapter 5 and is as shown in (6.13). The source-affected closed-loop output admittance can be calculated as in (6.14).

$$Y_{o-c}^{\text{out-in}} = \frac{Y_{o-o}}{(1 + L_{\text{out}})(1 - L_{\text{in}})} - \frac{L_{\text{in}}}{1 - L_{\text{in}}} Y_{o-\infty} \quad (6.13)$$

$$Y_{o-c}^S = \frac{1 + Z_{\text{in-oco}}^{\text{in-out}} Y_S}{1 + Z_{\text{in-c}}^{\text{in-out}} Y_S} Y_{o-c}^{\text{in-out}}, \quad (6.14)$$

where

$$Z_{\text{in-oco}}^{\text{in-out}} = Z_{\text{in-c}}^{\text{in-out}} + \frac{G_{\text{io-c}}^{\text{in-out}} T_{\text{oi-c}}^{\text{in-out}}}{Y_{o-c}^{\text{in-out}}} \quad (6.15)$$

is the open circuit input impedance at closed loop.

The output admittance was measured as an impedance and is shown in Fig. 6.10. The impedance had the same characteristics in all operation points and only the one measured in the CC region is shown. Output impedance in the CV region and MPP are shown in Appendix B.

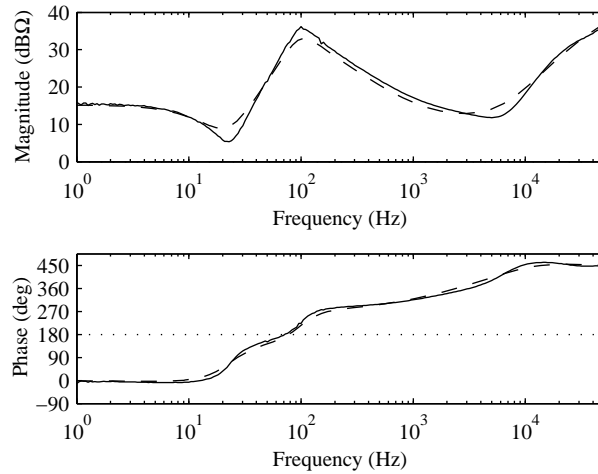


Figure 6.10: Predicted (dashed) and measured (solid) output impedances at closed loop in the CC region.

An important observation from Fig. 6.10 is that the phase of the output impedance crosses -180° at frequency around 80 Hz. Since the dc-equivalent model imitates the

behavior of the inverter model in the synchronous frame, the same behavior is present in the three-phase inverter. This could lead to instability according to minor-loop gain, introduced by Middlebrook [34]: if the grid impedance equals the output impedance in magnitude and the phase difference of these two impedances equals 180° , the system will become unstable.

The phase behavior in all operating points is virtually the same. This means that the photovoltaic generator itself does not cause the negative output impedance. Thus it is a property of the used control system and originates from the fact that the control signal of the voltage controller has to be inverted. The rest of the measured output impedances are collected in Appendix B. The appearance of negative output impedance was reported earlier in [35–37]. This could be a consequence of cascade control system, but not enough information about the used inverter models were given to verify this. The negative resistor like behavior appears between the crossover frequencies of voltage and current loops. This can be deduced also from (6.13), where the term $Y_{o-\infty}$ dominates the low frequency behavior of the output admittance. In the frequencies where the gain of the input control loop is high, the minus sign is cancelled by the denominator. In the vicinity of the input-voltage control crossover frequency, the gain of the input control loop is low and the minus sign appears.

The PV generator was approximated by a parallel connection of a photocurrent source and a dynamic resistance, because the dynamic resistance models the terminal behavior of the PV generator it does not contribute to the measured input impedance. The input impedance of the converter can be calculated to be as shown in (6.16).

$$Z_{in-c} = \frac{Z_{in-o}}{(1 + L_{out})(1 - L_{in})} + \frac{L_{out}}{(1 + L_{out})(1 - L_{in})} Z_{in-\infty} \quad (6.16)$$

The measured and predicted closed-loop input impedances are shown in Fig. 6.11.

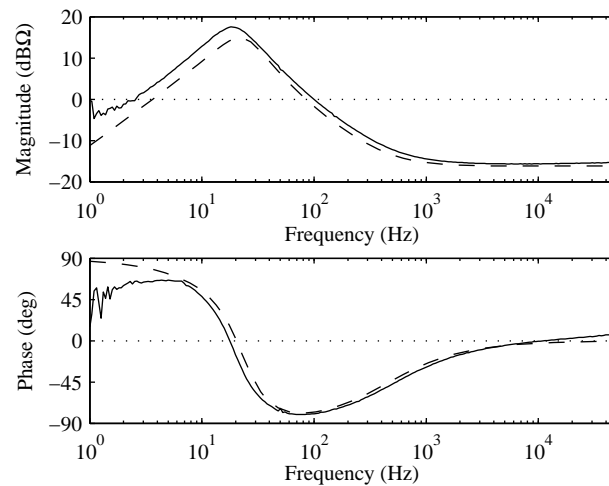


Figure 6.11: Predicted (dashed) and measured (solid) input impedances at closed loop.

The input impedance of the converter and the output impedance of the PV generator are compared in Fig. 6.12. The output impedance is shown in short-circuit (SC) and open-circuit (OC) conditions. It can be deduced that the minor loop related to input side interactions does not imply instability to take place: the magnitudes of the impedances coincide when the PV generator operates in the open circuit, but the phase difference is much less than 180° . The situation can however change if load interactions come into play but this subject is not treated in this thesis.

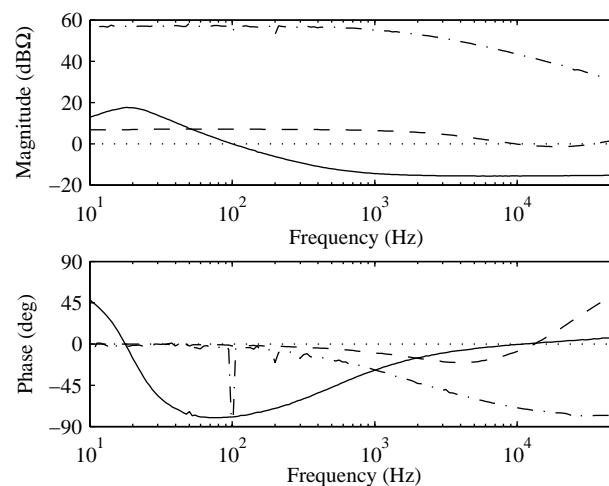


Figure 6.12: Measured closed-loop input impedance of the converter (solid) and output impedances of the PV module in short circuit (dash-dotted) and open circuit (dashed).

7. CONCLUSIONS

Small-signal modeling of a three-phase two-level grid-connected inverter can be done when the three-phase variables are transformed to a rotating synchronous reference frame. In a balanced and symmetrical grid, sinusoidal signals become dc-valued. This makes implementation of a control system easy, because the error signals can be compensated with PI controllers. In addition, the transfer functions, by means of which the controllers can be tuned, become available. The resulting control block diagram of an inverter in the synchronous reference frame is, however, quite complex and the required closed-loop transfer functions can not be easily solved.

In this thesis, a reduced-order model was constructed to approximate the dynamical properties of a grid-connected three-phase two-level inverter used in PV grid-interfacing. Approximation was done by assuming ideal grid voltages and neglecting the cross-coupling terms resulting from the space-vector transformation. The reduced-order model can be used to study the behaviour of the inverter in different operating points along the PV generator I - U -curve by including the source effect. This is done by approximating the PV generator as a parallel combination of a photocurrent source and a resistor. The value of the resistor depends on the operating point and is highest in the constant current region and lowest in the constant voltage region.

The PV generator has a major effect in the control design of the converter. It introduces a RHP-zero to control-to-output-current transfer function when the generator voltage is lower than the MPP voltage. This makes the phase experience a phase flip from zero to 180° when the generator voltage drops below the MPP. Single-loop output current control that is stable in all operation points is therefore impossible to implement.

A cascaded control structure has been widely adopted in three-phase inverters. Such a control structure consists of two loops connected in cascade. The inner loop controls the output current to be in phase with the grid voltage and the outer loop controls the input voltage to realize maximum power point tracking. In the literature, it is common to consider the dynamic properties of an inverter similar to those of a lossy inductor. In this case, the input voltage is assumed to be a constant and thus an input variable. In reality, the input voltage is determined by the current charging the input capacitor and the assumption of the constant input voltage is not correct.

In this work, the input voltage was treated as a controllable output variable. The control-to-input-voltage transfer function implies that the control signal of the voltage controller needs to be inverted.

The most important observation, when using a cascaded control scheme, was the appearance of a negative output impedance independent. This can lead to instability

at the harmonic frequencies when the grid impedance matches the output impedance of the converter with a phase difference of 180° .

Future work will include measuring frequency responses from an actual three-phase inverter connected to a three-phase voltage load and studying the methods to avoid the appearance of the negative output impedance by means of proper control design.

BIBLIOGRAPHY

- [1] B. K. Bose, "Global warming: energy, environmental pollution, and the impact of power electronics," *IEEE Industrial Electronics Magazine*, pp. 6,17, March 2010. DOI: 10.1109/MIE.2010.935860.
- [2] M. Liserre, T. Sauter, and J. Y. Hung, "Future energy systems: Integrating renewable energy sources into the smart power grid through industrial electronics," *IEEE Industrial Electronics Magazine*, pp. 18,37, March 2010. DOI: 10.1109/MIE.2010.935861.
- [3] J. H. R. Enslin, "Opportunities in hybrid energy networks using power electronic interfaces," *International Conference on Future Power Systems*, pp. 1,7, 2005. DOI: 10.1109/FPS.2005.204212.
- [4] J. M. G. et. al., "Distributed generation: Toward a new energy paradigm," *IEEE Industrial Electronics Magazine*, pp. 52,64, March 2010. DOI: 10.1109/MIE.2010.935862.
- [5] R. C. Dorf and R. H. Bishop, *Modern Control Systems*. Addison-Wesley, 1995. ISBN: 0-201-84559-8.
- [6] S. H. et. al., "Comparative analysis of pi decoupling control strategies with or without feed-forward in srf for three-phase power supply," *International Conference on Electrical Machines and Systems, ICEMS*, pp. 2372,2377, 2008.
- [7] J. L. et. al., "Indirect digital control of three-phase dc/ac inverter," *7th International Conference on Electrical Engineering Computing Science and Automatic Control, CCE*, pp. 105,110, 2010. DOI: 10.1109/ICEEE.2010.5608565.
- [8] R. Kadri, J.-P. Gaubert, and G. Champenois, "An improved maximum power point tracking for photovoltaic grid-connected inverter based on voltage-oriented control," *IEEE Transactions on Industrial Electronics*, vol. 58, pp. 66,75, January 2011. DOI: 10.1109/TIE.2010.2044733.
- [9] M. G. Villalva, T. G. de Siqueira, and E. Ruppert, "Voltage regulation of photovoltaic arrays: small-signal analysis and control design," *Power Electronics, IET*, vol. 3, pp. 869,880, January 2010. DOI: 10.1049/iet-pel.2008.0344.
- [10] S. Hiti, D. Boroyevich, and C. Cuadros, "Small-signal modeling and control of three-phase pwm converters," *Industry Applications Society Annual Meeting*, pp. 1143,1150, 1994. DOI: 10.1109/IAS.1994.377572.
- [11] J. B. et. al., "A state-space model for the comprehensive dynamic analysis of three-level voltage-source inverters," *28th Annual IEEE Power Electronics Specialists Conference*, pp. 942,948, 1997. DOI: 10.1109/PESC.1997.616837.

- [12] A. Yazdani and P. P. Dash, "A control methodology and characterization of dynamics for a photovoltaic (pv) system interfaced with a distribution network," *IEEE Transactions on Power Delivery*, vol. 24, pp. 1538,1551, July 2009. DOI: 10.1109/TPWRD.2009.2016632.
- [13] A.Mäki, S. Valkealahti, and T. Suntio, "Dynamic terminal characteristics of a photovoltaic generator," *14th International Power Electronics and Motion Control Conference, EPE-PEMC*, pp. 76,80, 2010.
- [14] R. Erickson and D. Maksimovic, *Fundamentals of Power Electronics*. Springer Science+Business Media, 2004. ISBN: 978-0-7923-7270-7.
- [15] R. Middlebrook and S. Cuk, "A general unified approach to modelling switching-converter power stages," *Power Electronics Specialists Conference*, pp. 18,34, 1976.
- [16] G. Wester and R. Middlebrook, "Low-frequency characterization of switched dc-dc converters," *IEEE Transactions on Aerospace and Electronic Systems*, vol. AES-9, pp. 376,385, May 1973.
- [17] T. Suntio, *Dynamic Profile of Switched-Mode Converter*. Wiley-VCH, 2009. ISBN: 978-3-527-40708-8.
- [18] C. K. Tse, *Linear Circuit Analysis*. Addison-Wesley, April 1998. ISBN: 0-201-34296-0.
- [19] J. Ollila, *Analysis of PWM-converters using space vector theory - application to a voltage source rectifier*. PhD thesis, Tampere University of Technology, 1993. Tampere.
- [20] K. P. Kovacs and I. Racz, *Transiente Vorgänge in Wechselstrommaschinen, Band I*. Verlag der Ungarischen Akademie der Wissenschaften, 1959. Budabest,Hungary.
- [21] E. F. et. al., "Sensitivity study of the dynamics of three-phase photovoltaic inverters with an lcl grid filter," *IEEE Transactions on Industrial Electronics*, vol. 56, pp. 706,717, March 2009.
- [22] N. Mohan, T. Undeland, and W. Robbins, *Power Electronics*. John Wiley & Sons, Inc, 2003. ISBN: 0-471-42908-2.
- [23] F. Blaabjerg, R. Teodorescu, M. Liserre, and A. Timbus, "Overview of control and grid synchronization for distributed power generation systems," *IEEE Transactions on Industrial Electronics*, vol. 53, pp. 1398,1409, October 2006. DOI: 10.1109/TIE.2006.881997.
- [24] A. S. Khalifa and E. F. El-Saadany, "Control of three phase grid connected photovoltaic power systems," *14th International Conference on Harmonics and Quality of Power (ICHQP)*, pp. 1,7, 2010.

- [25] W. X. et. al., "Regulation of photovoltaic voltage," *IEEE Transactions on Industrial Electronics*, vol. 54, pp. 1365,1374, June 2007. DOI: 10.1109/TIE.2007.893059.
- [26] A. Yazdani and R. Iravani, *Voltage-Sourced Converters in Power Systems: Modeling, Control, and Applications*. John Wiley & Sons, Inc, 2010. ISBN: 978-0-470-52156-4.
- [27] I. S. 929-2000, *IEEE Recommended practice for utility interface of photovoltaic (PV) systems*. April 2000. ISBN: 0-7381-1934-2 SH94811.
- [28] H. Mao, D. Broyevich, and F. C. Y. Lee, "Novel reduced-order small-signal model of a three-phase pwm rectifier and its application in control design and system analysis," *IEEE Transactions on Power Electronics*, vol. 13, pp. 511,521, May 1998.
- [29] C. T. Rim, D. Y. Hu, and G. H. Cho, "Transformers as equivalent circuits for switches: general proofs and d-q transformation-based analyses," *IEEE Transactions on Industry Applications*, vol. 26, pp. 777,785, July/August 1990.
- [30] M. Routimo, *Developing a voltage-source shunt active power filter for improving power quality*. PhD thesis, Tampere University of Technology, 2008. Tampere.
- [31] A. Y. et. al., "Modeling guidelines and a benchmark for power system simulation studies of three-phase single-stage photovoltaic systems," *IEEE Transactions on Power Delivery*, vol. 26, pp. 1247,1264, April 2011. DOI: 10.1109/TPWRD.2010.2084599.
- [32] T. S. et. al., "Issues on solar-generator interfacing with current-fed mpp-tracking converters," *IEEE Transactions on Power Electronics*, vol. 25, pp. 2409,2419, September 2010.
- [33] J. Maciejowski, *Multivariable Feedback Design*. Addison-Wesley, 1989. ISBN: 0-201-18243-2.
- [34] R. D. Middlebrook, "Input filter considerations in design and application of switching regulators," in *Proc. IEEE Industry Applications Society*, pp. 91,107, 1976.
- [35] K. Visscher and P. J. M. Heskes, "A method for operational grid and load impedance measurements," *International Conference on Future Power Systems*, pp. 1,4, 2005. DOI: 10.1109/FPS.2005.204324.
- [36] P. J. M. Heskes, J. M. A. Myrzik, and W. L. Kling, "Harmonic distortion and oscillatory voltages and the role of negative impedance," *Power and Energy Society General Meeting, IEEE*, pp. 1,7, 2010. DOI: 10.1109/PES.2010.5588137.

-
- [37] J. H. R. Enslin and P. J. M. Heskes, “Harmonic interaction between a large number of distributed power inverters and the distribution network,” *IEEE Transactions on Power Electronics*, vol. 19, pp. 1586,1593, November 2004. DOI: 10.1109/TPEL.2004.836615.

A. COMPARISON OF INVERTER AND REDUCED ORDER MODELS

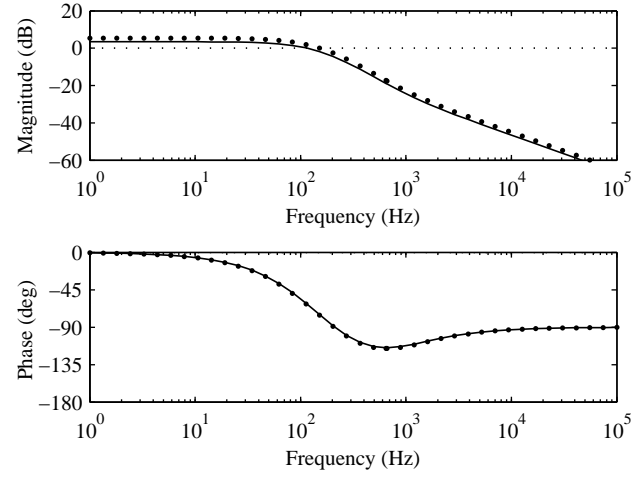


Figure A.1: Estimated output-to-input transmittances from inverter dq-model (dotted line) and reduced order dc-dc model (solid line).

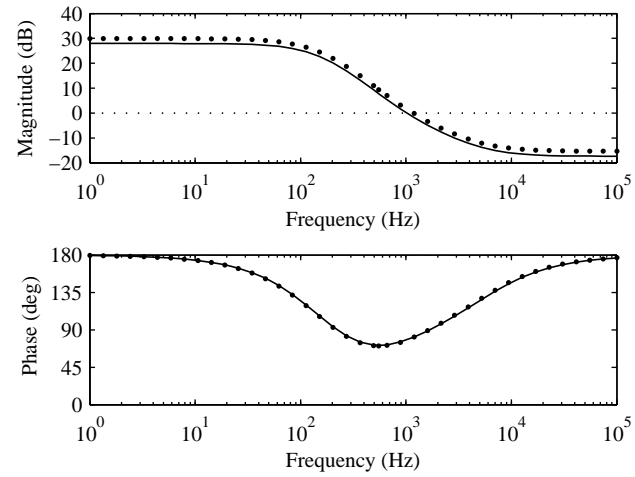


Figure A.2: Estimated control-to-input transfer functions from inverter dq-model (dotted line) and reduced order dc-dc model (solid line).

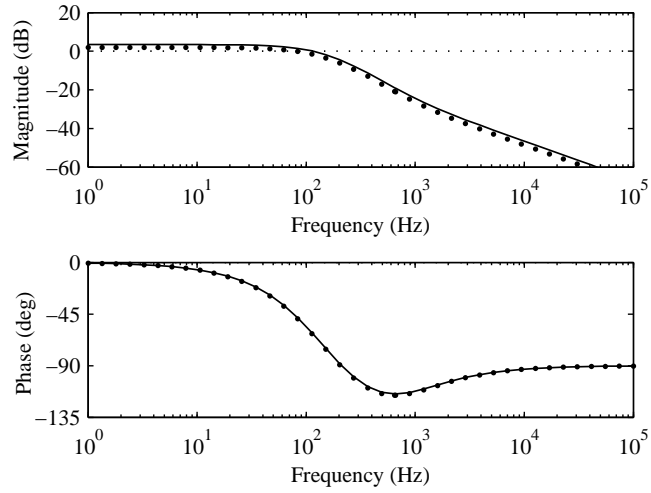


Figure A.3: Estimated input-to-output transfer functions from inverter dq-model (dotted line) and reduced order dc-dc model (solid line).

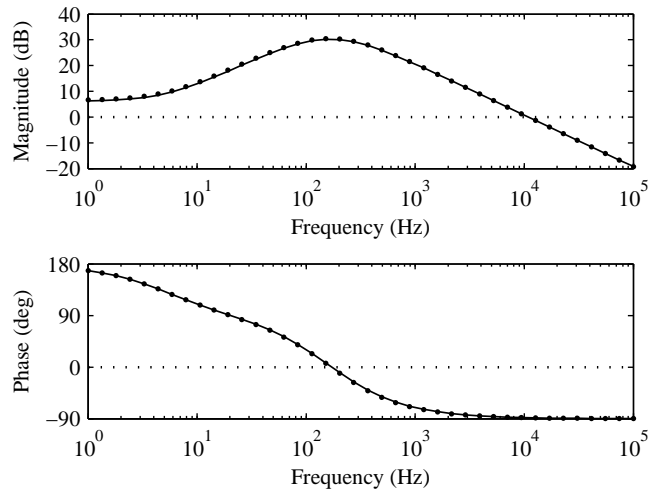


Figure A.4: Estimated control-to-output transfer functions from inverter dq-model (dotted line) and reduced order dc-dc model (solid line).

B. CLOSED-LOOP OUTPUT IMPEDANCES OF DC-EQUIVALENT CIRCUIT

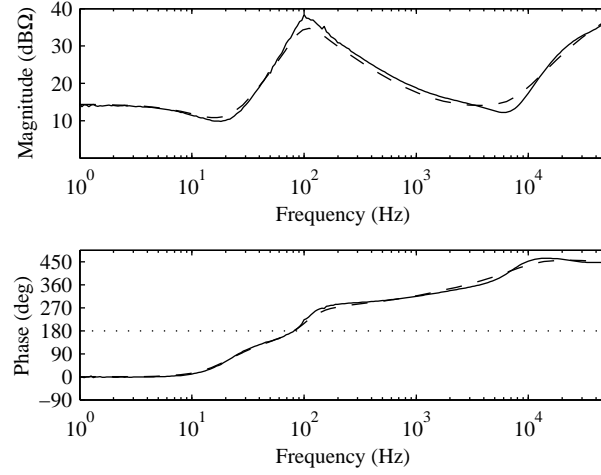


Figure B.1: Predicted and measured output impedances of the dc-dc equivalent converter in MPP at closed-loop.

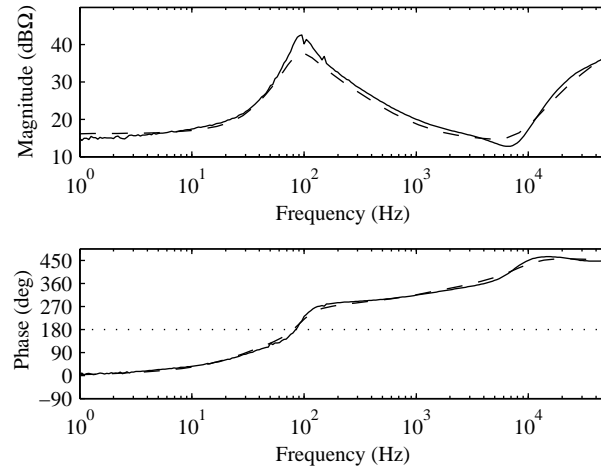


Figure B.2: Predicted and measured output impedances of the dc-dc equivalent converter in CV region at closed-loop.

C. PROTOTYPE CONVERTER

The power-stage of the prototype converter is depicted in Fig. C.1 and the final assembled converter in Fig. C.2.

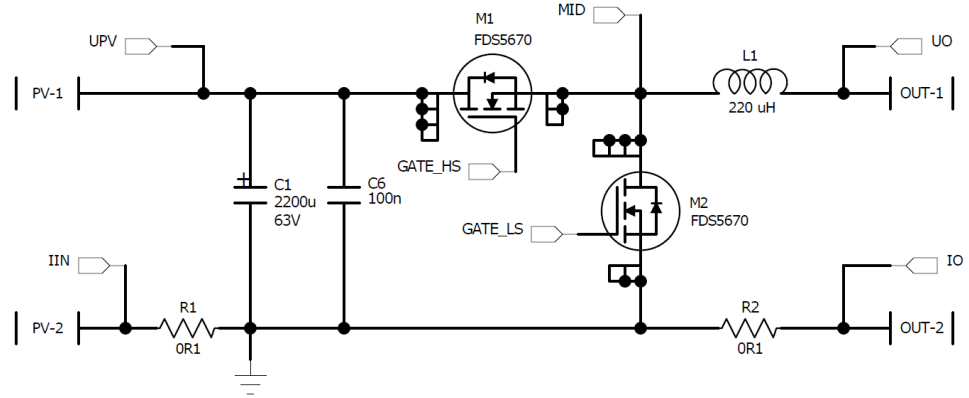


Figure C.1: Power-stage of the prototype converter.

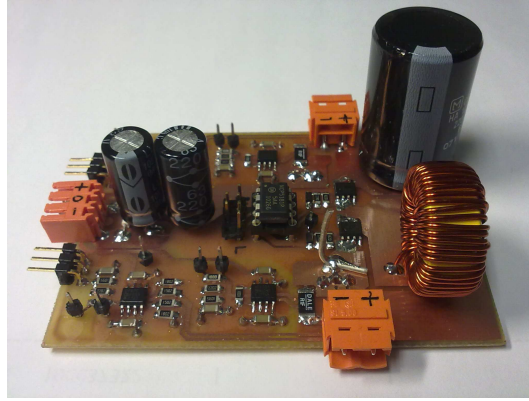


Figure C.2: Prototype converter.

The measurement circuits were designed to give output voltages less than 3 V to protect the DSP from overvoltage. Output current measurement circuit was implemented using an instrument amplifier and a passive low-pass filter as depicted in Fig. C.3. The input voltage measurement was done using a differential amplifier circuit and low-pass filtering as shown in Fig. C.4.

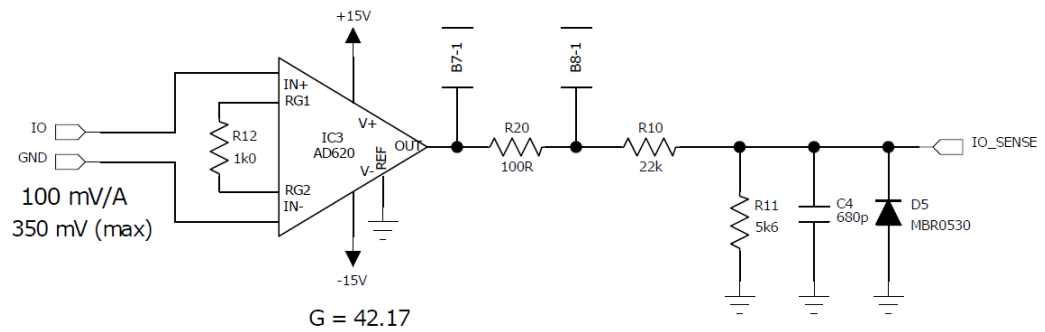


Figure C.3: Output current sensing measurement circuit.

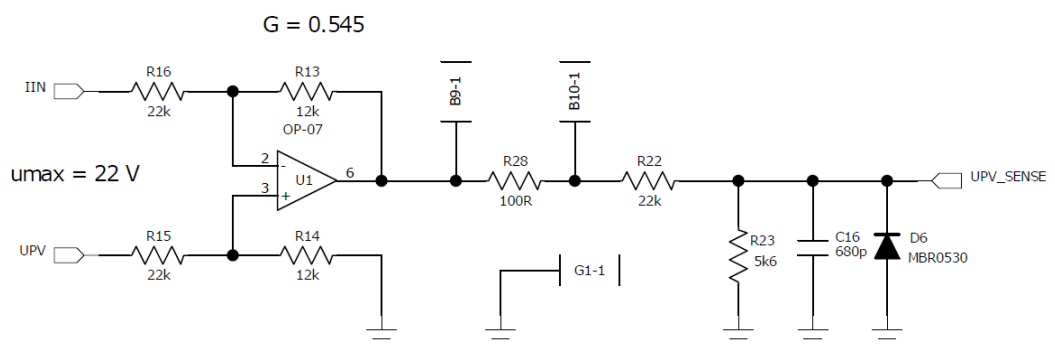


Figure C.4: Input voltage sensing measurement circuit.